

Galaxy Secular Mass Flow Rate Determination Using the Potential-Density Phase Shift Approach

X. Zhang¹* and R. J. Buta²

¹Department of Physics and Astronomy, George Mason University, 4400 University Drive, Fairfax, VA 22030, USA

²Department of Physics and Astronomy, University of Alabama, 514 University Blvd E, Box 870324, Tuscaloosa, AL 35487, USA

Accepted . Received ; in original form

ABSTRACT

We have carried out an initial study of a small sample of nearby spiral and barred galaxies with a broad distribution of Hubble types in order to have a first estimate of the magnitude of their secular mass accretion/excretion rates in the context of bulge building and morphological evolution along the Hubble sequence. The stellar surface density maps of the sample galaxies were derived from the archival data of the *Spitzer* Infrared Nearby Galaxies Survey (SINGS), as well as the Sloan Digital Sky Survey (SDSS). The corresponding molecular and atomic surface densities were derived from archival CO(1-0) and HI interferometric observations of the BIMA SONG, THINGS, and VIVA surveys. The method used for determining the radial mass flow rates follows from our previous work using the potential-density phase shift approach, which utilizes a volume-type torque integral to calculate the angular momentum exchange rate between the basic state disk matter and the density wave modes. This volume-type torque integral is shown to contain the contributions from both the gravitational torque couple and the advective torque couple at the nonlinear, quasi-steady state of the wave modes, in sharp contrast to its behavior in the linear regime, where it contains only the contribution from the gravitational torque couple as was shown by Lynden-Bell & Kalnajs in 1972. The phase-shift/volume-torque method is shown to yield radial mass flow rates and angular momentum transport rates several times higher than similar rates estimated using the traditional method of gravitational torque couple of Lynden-Bell and Kalnajs, and this difference reflects the dominant role played by collisionless shocks in the secular evolution of galaxies containing extremely non-linear, quasi-steady density wave modes. It is shown that these non-linear modes maintains their quasi-steady state at the expense of a continuous radial mass flow and the resulting morphological transformation of galaxies throughout their lifetime, not only for late-type and intermediate-type disk galaxies but, under favorable conditions, also for earlier types including S0s and disky ellipticals. Enabling this transformation along the entire Hubble sequence, we show here for the first time using observational data that *stellar* mass accretion/excretion is just as important, and oftentimes much more important, than the corresponding accretion/excretion processes in the *gaseous* component, with the latter being what had been emphasized in most of the past secular evolution studies. We address the implications of our result in the context of the cosmological evolution of galaxies, as well as the challenges it poses to the standard Lambda Cold Dark Matter (LCDM) paradigm. We also point out the connection between the large-scale collective dissipation process enabled by the galactic density wave modes to similar processes happening in fluid turbulence and in symmetry breaking processes in fundamental physics, which places the galaxy evolution study in the context of the general studies of complex, nonequilibrium systems.

Key words: galaxies: evolution; galaxies: formation; galaxies: spiral

1 INTRODUCTION

The possibility that galaxy morphologies can transform significantly over their lifetime, not only through violent

* E-mail: xzhang5@gmu.edu

episodes such as merger and satellite accretion, but also through slow and steady internal secular dynamical processes, is an idea that has been gaining acceptance in recent decades. In the past, work on secular evolution has been focused on gas accretion in barred galaxies and the growth of pseudo (disk-like) bulges (Kormendy & Kennicutt 2004, hereafter KK04, and references therein). This is partly due to the long-held notion, naturally expected in the classical mechanics of few-body systems developed since Newton's time and refined throughout the 18th and 19th century, that gas is the only mass component capable of dissipation, while the stellar component is adiabatic, and generally does not lose or gain energy and angular momentum as stars orbit around the center of a galaxy. This view, however, is expected to be challenged in view of parallel developments in other physical systems such as atmospheric convection flow, chemical clocks, and turbulence in fluid dynamics, where the interaction of the multitudes of degree-of-freedom in these complex, nonlinear and nonequilibrium systems leads to the emergence of chaos and cooperative behavior (i.e. self-organized, large-scale non-equilibrium patterns that break the symmetry of the parent systems). The emergence of self-organized global patterns are often accompanied by the emergence of new meta-laws governing the evolution of these complex systems, a characteristic that has been revealed not only in the classical complex systems, but more prevalently in the quantum domain which dominates the studies of the foundations of physics.

The indication that there is the possibility of significant secular *stellar mass redistribution* in galaxies in fact already appeared in the seminal work of Lynden-Bell and Kalnajs (1972, hereafter LBK), who showed that a trailing spiral density wave possesses a gravitational torque that over time can transport angular momentum outward. LBK were interested in the angular momentum transport phenomenon because they were seeking a generating mechanism for the spiral density waves, thought at the time to have a longevity of the order of 10^9 years because of the radial group velocity discovered by Toomre (1969), which resulted in their propagation and eventual absorption at the inner Lindblad resonance (thus the reason for the title of the LBK paper: "On the Generating Mechanism of Spiral Structure"). Since the density wave is considered to possess negative energy and angular momentum density inside corotation relative to the basic state (i.e. the axisymmetric disk, see, e.g. Shu [1992], Chapters 11 and 12 for the fundamentals of density wave theory), an outward angular momentum transport from the inner disk would encourage the spontaneous growth of the wave trains. LBK at that time were not interested in the secular morphological evolution of the basic state of the disks. In fact, in the same paper, they showed that for WKBJ (tightly wrapped) waves, the long-term energy and angular momentum exchange between a *quasi-steady* wave train and the basic state is *identically zero* away from the wave-particle resonances, thus much of the basic state of the disk does not experience secular mass redistribution according to their theory. That this zero-exchange between the wave and the disk matter is possible, in the presence of the outward angular momentum transport by gravitational torque couple, is because there is a second type of torque couple, the so-called advective torque couple (due to lorry transport, or Reynolds stress, see §6 of LBK paper for more detailed

explanation), that opposes the gravitational torque couple, and the sum of the two types of torque couples is a constant independent of galactic radius (LBK, see also Binney & Tremaine 2008, hereafter BT08, pp. 492). The total torque couple, which is equal to the rate of angular momentum flux, is thus a constant in their theory during the outward radial transport of angular momentum, and there is no interaction of the wave and the basic state except at the wave-particle resonances (i.e., LBK thought the wave picks up angular momentum from the basic state at the inner Lindblad resonance and dumps it at the outer Lindblad resonance, and *en route* of this radial transport the total angular momentum flux remains constant). Strickly speaking, LBK proved these results only for WKBJ (tightly-wrapped) waves, and they have also taken the zero-growth (steady wave) limit.

Zhang (1996, 1998, 1999, hereafter Z96, Z98, Z99) showed that the classical theory of LBK ignored an important collective dissipation process¹ present in the gravitational N-body disks possessing *self-organized, or spontaneously-formed, density wave modes*. This process is mediated by collisionless shocks at the density wave crest, which breaks the adiabaticity or the conservation of the Jacobi integral condition – a condition which was shown to be valid only for a *passive* orbit under an *applied* steady spiral or bar potential (BT08, p. 179), and is now shown not to be obeyed by orbits undergoing collective dissipation as is applicable for a self-sustained or self-organized spiral or bar modes. The overall manifestation of the collective dissipation process is an azimuthal phase shift between the potential and the density distributions of the density wave pattern, and for a self-sustained mode, the radial distribution of phase shift is such that it is positive inside corotation and negative outside (Z96, Z98). The presence of the phase shift means that for every annulus of the galaxy, there is a secular torque applied by the density wave on the disk matter in the annulus, and the associated energy and angular momentum exchange between the wave mode and the basic state of the disk at the nonlinear, quasi-steady state of the wave mode (in the linear regime, the same phase shift distribution leads

¹ The phrases "collective dissipation" or "collective effects" we adopted in describing the galactic density wave dynamics attempt to describe a general tendency for non-equilibrium, self-organized coherent structures to spontaneously generate emergent global dynamics through the local interactions of subsystems. Other phrases used in this context in the literature, ranging in applications including condensed matter physics, fluid dynamics, economics and social sciences, include "cooperative effect", "coupling and interaction among the degrees-of-freedom of a complex system". A not entirely fitting analogy of collective versus hierarchical control is the difference between a democracy and a dictatorship. A democracy functions through the interactions of sub-entities but ultimately is controlled by the innate dynamical forces of society and history, whereas a dictatorship in its ultimate form exerts a top-down control with no lateral influence among the subunits. In the case of a galaxy possessing a density wave pattern, a top-down control would be for orbits to respond entirely *passively* to an *applied* potential, whereas the collective point of view allows us to take into account new physics emergent from the mutual interactions of N-particles in the galaxy, which on the other hand is implicitly determined by the innate dynamics of such a system to spontaneously form self-organized global instabilities when the boundary condition is right.

to the spontaneous emergence of the wave mode. See Z98). As a result, the disk matter inside corotation (both stars and gas) loses energy and angular momentum to the wave, and spirals inward, and the disk matter outside corotation gains energy and angular momentum from the wave and spirals outward. *This energy and angular momentum exchange between the wave and the basic state of the disk thus becomes the ultimate driving mechanism for the secular evolution of the mass distribution of the basic state of galaxy disks.* The energy and angular momentum received by the wave from the basic state, incidentally, also serve as a natural damping mechanism for the spontaneously growing unstable mode, allowing it to achieve quasi-steady state at sufficiently nonlinear amplitude Z98). In other words, the density wave pattern achieves a state of *dynamical equilibrium* at the expense of a continuous flux of matter, energy, and entropy through the system, with the local entropy production balanced by entropy export by the pattern (thus no local entropy increase, as evidenced by the steady wave amplitude), but with the overall entropy increase of the combined system of the pattern plus the environment: a condition satisfied by similar kind of nonequilibrium dissipative structures in nature (Nicolis & Prigogine 1977).

In Z98, a set of analytical expressions for the secular mass accretion/excretion rate was derived, and was confirmed quantitatively in the N-body simulations presented in the same paper. However, due to the two-dimensional nature of these simulations, where the bulge and halo were assumed to be spherical and inert, the simulated wave mode has an average arm-to-interarm density contrast of 20% and potential contrast of 5%, both much lower than the commonly observed density wave contrast in physical galaxies, so the simulated disk did not evolve much (Z99), despite the fact that these low evolution rates conform exactly to the analytical formula's prediction of the mass flow rate for the corresponding (low) wave amplitude (Z98, section 5.2). Incidentally, the evolution rate given by this theory is proportional to the wave amplitude squared, so a change from 10% average wave amplitude to 30% average wave amplitude is almost a factor of 10 difference in effective secular mass flow rate.

Since state-of-the-art N-body simulations have yet to reproduce the extremely nonlinear density wave amplitudes in observed physical galaxies, an alternative to confirming the magnitude of the secular evolution effect using numerical simulations, is to use observed near- and mid-infrared images directly as tracers of galaxy mass, and apply the analytical formalism of Z96, Z98 to these observationally-derived surface density maps to derive secular mass flow rates. As a first step, Zhang & Buta (2007, hereafter ZB07) and Buta & Zhang (2009, hereafter BZ09) used near-infrared images of more than 150 observed galaxies to derive the radial distribution of the azimuthal potential-density phase shifts, and to use the positive-to-negative (P/N) zero crossings of the phase shift curve to determine the corotation radii (CRs) for galaxies possessing spontaneously-formed density wave modes. This approach works because the alternating positive and negative humps of phase shift distribution lead to the correct sense of energy and angular momentum exchange between the wave mode and the disk matter to encourage the spontaneous emergence of the mode (Z98). In ZB07 and BZ09, we have found good correspondence between the pre-

dicted CRs using the potential-density phase shift approach, and the resonance features present in galaxy images, as well as with results from other reliable CR determination methods within the range of validity of these methods. Besides CR determination, an initial test for mass flow rate calculation, for galaxy NGC 1530, was also carried out in ZB07 using the same volume-torque-integration/potential-density phase shift approach. We found there that since NGC 1530 has exceptionally high surface density, as well as extremely-large arm-to-interarm contrast, mass flow rates of more than 100 solar masses per year were obtained across much of the disk of this galaxy. This level of mass flow rate, if sustainable, is more than sufficient to transform the Hubble type of a late type galaxy to an early type (i.e. S0 or disk elliptical) within a Hubble time.

Recently, we have applied the potential-density phase shift/volume-torque method to an initial sample of disk galaxies of varying Hubble types in order to study various issues relating to the secular mass redistribution and Hubble-type transformation. In what follows, we apply the potential-density phase shift/volume-torque method to our initial sample of disk galaxies with varying Hubble types in order to estimate the mass flow rates for both stars and gas, and to compare their relative importance.

2 THEORETICAL BASIS FOR APPLYING THE POTENTIAL-DENSITY PHASE SHIFT APPROACH TO THE MASS FLOW RATE CALCULATION

The detailed discussion on the collective dissipation mechanism responsible for the secular redistribution of both stellar and gaseous mass in galaxies can be found in Z96, Z98, Z99. In ZB07 and BZ09, procedures for calculating the radial distribution of potential-density phase shift of the density wave patterns using observed infrared images are described. A similar procedure, with slight modification, will be used for the calculation of the mass flow rates in the current paper. We now briefly summarize the theoretical derivations relevant to these calculations.

For pedagogical purposes we will derive the equation for mass flow rate through the orbit decay rate of an average star under the action of a density wave mode. The (inward) radial mass accretion rate at a galactic radius R is related to the mean orbital decay rate $-dR/dt$ of an average star through

$$\frac{dM(R)}{dt} = -\frac{dR}{dt} 2\pi R \Sigma_0(R) \quad (1)$$

where $\Sigma_0(R)$ is the mean surface density of the basic state of the disk at radius R .

We also know that the mean orbital decay rate of a single star is related to its angular momentum loss rate dL^*/dt through

$$\frac{dL^*}{dt} = -V_c M_* \frac{dR}{dt} \quad (2)$$

where V_c is the mean circular velocity at radius R , and M_* the mass of the relevant star.

Now we have also

$$\frac{dL^*}{dt} = \overline{\frac{dL}{dt}}(R) \frac{M_*}{\Sigma_0} \quad (3)$$

where $\frac{dL}{dt}(R)$ is the angular momentum loss rate of the basic state disk matter per unit area at radius R.

Since

$$\frac{dL}{dt}(R) = \frac{1}{2\pi} \int_0^{2\pi} \Sigma_1 \frac{\partial \mathcal{V}_1}{\partial \phi} d\phi \quad (4)$$

(Z96), we have finally

$$\frac{dM(R)}{dt} = \frac{R}{V_c} \int_0^{2\pi} \Sigma_1 \frac{\partial \mathcal{V}_1}{\partial \phi} d\phi \quad (5)$$

where the subscript 1 denotes the perturbation quantities. This result, even though derived through the stellar orbital decay rate, is in fact general, and can be applied to the mass accretion rate of both stars and gas, as long as the relevant perturbation surface density is used. And we note that the potential perturbation to be used for the calculation of either the stellar or gaseous accretion needs to be that of the total potential of all the mass components, since the accretion mass cannot separate the forcing field component, and responds only to the total forcing potential.

In the above derivation we have used a volume-type of torque $T_1(R)$,

$$T_1(R) \equiv R \int_0^{2\pi} \Sigma_1 \frac{\partial \mathcal{V}_1}{\partial \phi} d\phi, \quad (6)$$

which was first introduced in Z96 and Z98 in the context of the self-torquing of the disk matter in a unit-width annulus at R by the potential of the associated spontaneously-formed density wave mode. The volume torque is equal to the time rate of angular momentum exchange between the density wave and the disk matter in a unit-width annulus at R, for wave modes in approximate quasi-steady state. In the past, two other types of torque-coupling integrals have also been used (LBK; BT08). These are the gravitational torque couple $C_g(R)$

$$C_g(R) = \frac{R}{4\pi G} \int_{-\infty}^{\infty} \int_0^{2\pi} \frac{\partial \mathcal{V}}{\partial \phi} \frac{\partial \mathcal{V}}{\partial R} d\phi dz, \quad (7)$$

and the advective torque couple $C_a(R)$

$$C_a(R) = R^2 \int_0^{2\pi} \Sigma_0 V_R V_\phi d\phi, \quad (8)$$

where V_R and V_ϕ are the radial and azimuthal velocity perturbation relative to the circular velocity, respectively.

In the classical theory, the volume torque integral $T_1(R)$ can be shown to be equal to dC_g/dR in the linear regime (see Appendix A2 of Z98, original derivation due to S. Tremaine, private communication). However, for spontaneously-formed density wave modes, when the wave amplitude is significantly nonlinear and the importance of collisionless shocks at the density wave crest begins to dominate, it was shown in Z98 that one of the crucial conditions in the proof of the $T_1(R) = dC_g/dR$ relation, that of the validity of the differential form of the Poisson equation, is no longer valid. At the quasi-steady state (QSS) of the wave mode, it was shown in Z99 that in fact $T_1(R) = d(C_a + C_g)/dR \equiv dC/dR$! An intuitive derivation of this equality can be given as follows: $d(C_a + C_g)/dR \equiv dC/dR$ is the gradient of total wave angular momentum flux in the Eulerian picture, and $T_1(R)$ is the rate of angular momentum loss by the disk matter to the wave potential in a unit-width annulus located at R in the

Lagrangian picture. At the quasi-steady state of the wave mode, these two need to balance each other so the wave amplitude does not continue to grow (i.e., all the negative angular momentum deposited by the wave goes to the basic state of the disk matter and none goes to the wave itself, so that the wave amplitude does not continue to grow, as required by the condition for the quasi-steady state of the wave mode).

The past calculations of the secular angular momentum redistribution rate (i.e. Gnedin et al. [1995], Foyle et al. [2010]) considered only the contribution from gravitational torque couple and ignored the contribution of the advective torque couple (which cannot be directly estimated using the observational data, except through our round-about way of estimating the total torque using the volume-type of torque integral $T_1(R)$, and then subtracting from it the contribution of the gravitational torque to arrive at the contribution of the advective torque). Later in this paper, we will show that for the kind of density wave amplitudes usually encountered in observed galaxies, the advective contribution to the total torque in fact is several times larger than the contribution from the gravitational torque. Furthermore, in the nonlinear regime the advective torque couple is of the same sense of angular momentum transport as the gravitational torque couple – another characteristic unique to the nonlinear mode. Past calculations of gas mass accretion near the central region of galaxies (e.g. Haan et al. 2009) are likely to have significantly underestimated the gas mass flow rate for the same reason.

Later in this paper, we will also show that the density wave modes in observed galaxies show predominantly a kind of two-humped shape for the volume torque distribution (with zero crossing of the two humps located at CR). This two-humped distribution of the volume torque is equivalent to the two-humped distribution of the phase shift because the phase shift is defined through the volume torque (Z98). In ZB07 and ZB09, we found that galaxies often possess nested modes of varying pattern speeds, and each modal region has its own well-defined two-humped phase shift distribution. The constant pattern speed regime is delineated between the negative-to-positive (N/P) crossings of the adjacent modes, with the P/N crossing, or CR, sandwiched in between. The two-humped volume-torque or phase shift distribution is consistent with (and a direct result of) the bell-shaped torque couplings previously found in both N-body simulations (Z98, for gravitational, advective, and total torque couplings), and in observed galaxies (Gnedin et al. 1995² for gravitational torque coupling only). These charac-

² A little clarification on the chronologies of these early works appear in order. In the late 80's Zhang carried out initial studies of the possible dynamical mechanisms for the secular redistribution of galaxy matter and summarized the results of these early work in her PhD thesis (Zhang 1992). During the 1994 the Hague IAU general assembly she discussed this work with the then Princeton graduate student J. Rhodes, who requested preprints from her. She sent Rhodes the three draft papers that eventually published as Z96, Z98, Z99 in ApJ. Rhodes showed these papers to his professors Jeremy Goodman and David Spergel, who both showed great interests. Goodman subsequently asked his then graduate student O. Gnedin to begin a study of spiral torques in galaxy M100 using the approach of LBK, which was later published as

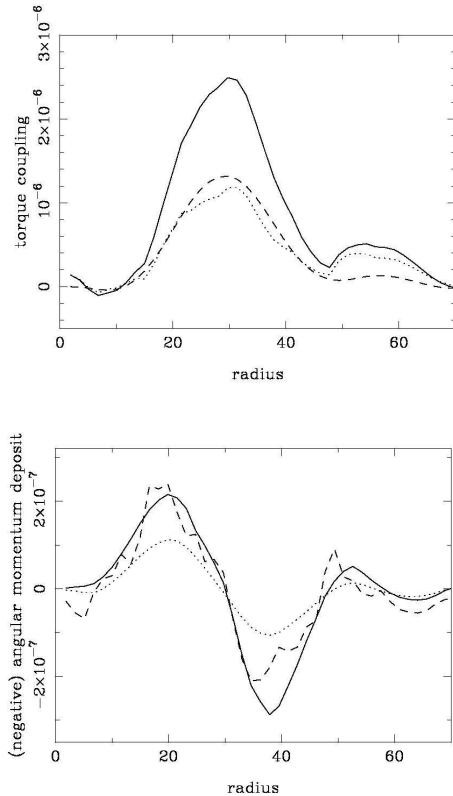


Figure 1. Top: Gravitational (dotted), advective (dashed), and total (solid) torque couples from the N-body simulations of Z96, Z98. Bottom: Gradient of gravitational (dotted) and total (dashed) torque couples, and the volume torque T_1 (solid), from the same N-body simulations (previously unpublished).

teristic distributions are another important piece of evidence that the density waves present in disk galaxies are in fact spontaneously-formed unstable modes in the underlying basic state of the disks (Z98 §3.4).

In Figure 1, we show the result of an N-body simulation from Z96, Z98. The top frame, which displays the various torque couplings, shows curves which have the characteristic bell-shapes that we have commented above. The peaks of the bell curves are near the CR of the dominant spiral mode in this simulation, at $r=30$. In the bottom frame, we show the calculated *gradient* of the gravitational and total torque couples, and compare them with $T_1(R)$, using quantities from the same set of N-body simulation. It is clear that $T_1(R) \neq dC_g/dR$, and rather is closer to dC/dR , though the equality is not yet exact because this particular simulated N-body mode never achieved true steady state. The shallower second bell-shape in the top frame (which corresponds to the second positive-followed-by-negative-hump feature in the bottom frame) is due to a spurious edge mode. In physical galaxies, as our examples below will show, the difference

Gnedin et al. (1995). The three papers by Zhang, however, experienced significant delays (including resubmissions) in the refereeing process, and thus came out after the Gnedin et al. paper, even though the latter work was carried out due to the direct influence of the former.

between $T_1(R)$ and dC_g/dR becomes even more pronounced than in these N-body simulations, due to the higher degree of nonlinearity of the wave modes in physical galaxies.

3 OBSERVATIONAL MOTIVATIONS FOR STUDYING SECULAR EVOLUTION ALONG THE HUBBLE SEQUENCE USING NEARBY SAMPLES OF DISK GALAXIES

As is well known, the original Hubble sequence was motivated by Hubble's early work in classifying nearby galaxies in order to find evolutionary connections among them according to the Jeans theory of the morphological evolution of galaxies (Jeans 1928). The original Jeans theory, however, got the evolution direction backwards, which apparently influenced Hubble's choice of the names for "early" and "late" type galaxies. With the observational evidence accumulated over the past few decades, we know now that galaxy morphological transformation generally proceeds along the Hubble sequence in the reverse direction (i.e. from late to early types), and this evolution generally takes a good fraction or longer of the entire age of the universe. The Hubble Deep and Ultra Deep Fields as well as many follow-on observations showed that high-z objects in general do not, at first sight, seem to conform to the classical Hubble classification. One might thus wonder: what is the rationale for studying the evolution along the Hubble sequence of nearby galaxies, since it is not clear that it would be relevant to the evolution of galaxies we observe across cosmic time?

We want to say at the outset that what we are trying to explore and establish is a broad trend that as the universe evolves, the galaxy population as a whole progressively evolves from disk-dominated systems to bulge-dominated systems. There is plenty of observational evidence now that the disk fraction was higher at $z = 1$ and has since decreased (Lilly et al. 1998). This is most naturally explained by secular evolution since the number density of galaxies of all types has not evolved much over the same time range (Cohen 2002), and the merger fraction since $z=1$ is low (Lopez-Sanjuan et al. 2009).

The next question is, what would serve as a natural starting point of secular evolution along the Hubble sequence? An obvious choice would be the very late type disks, i.e., Sd/Sc's, and low surface brightness galaxies (LSBs), since these are at the tail end of the Hubble sequence. One subtle point here is that the present-day LSB and late-type galaxies could not have been the ancestors of the present-day early-type galaxies, both due to their formation time difference and their statistical size/mass difference. We want, however, to bring up an analogy of the galaxy evolution scenario with the Darwinian evolution theory. According to this theory, humans evolved from an ape-like ancestor, but this is not the same as saying modern-day apes will one-day evolve into modern-day humans. This difference is the well-known distinction between an evolution-tree (which has historic connotation) and a ladder-of-life (which is used for present-day classification of species). The two phrases have close connections, but should not be confused with each other. For the problem of the secular evolution of galaxies, the same principle applies: we can fully envision that the ancestors of the present-day early-type galaxies were likely

to be disk systems much larger in size than present-day late-type disks, and they appear much earlier in the evolution history of the universe. Some of these early large disks may be the recently-discovered rotationally-supported high-z disks (Genzel et al. 2006; Ceverino et al. 2011), as well as the large rotationally-supported Damped Lyman Alpha (DLA) systems (Wolfe et al. 2005). Many of the fainter outer disks of these high-z systems may lie beyond detection (Hopkins et al. 2009), and thus we need to also take into account possible selection effects in interpreting high-z results (this aspect is related to the difficulty in detecting the high-z quasar host galaxies). The observed “down-sizing” trend of galaxy mass assembly (Cimatti et al. 2006; Nelan et al. 2005) also gives support to the idea that the first disk galaxies formed are likely to be larger ones.

There are theoretical reasons why galaxy evolution tend to proceed through a disk-phase, i.e., in a dissipative self-gravitating system the natural step of relaxation is first to settle onto a disk with the axis of rotation corresponding to the axis of maximum momentum of inertia (Zeldovich 1970). Such a system subsequently continues its entropy-increasing evolution towards the direction of increasing central concentration together with an extended outer envelope, and it gets rid of the excess angular momentum during this secular evolution process through the formation of large-scale collective instabilities (Z96). Besides considering purely gravitational processes for galaxy formation, it is essential to point out that we need also to take into account evidences that early galaxy formation may involve a significant role played by turbulence and supersonic shocks (Ozernoy 1974; Bershadskii & Screenivasan 2003; Zhang 2008 and the references therein). Incidentally, the primordial turbulence scenario for galaxy formation helps to eliminate one of the key reasons for the involvement of CDM in early galaxy formation, i.e. the smallness (10^{-5}) of initial seeds of perturbation on the cosmic microwave background (CMB), since the turbulence shock compression will form galaxies bypassing the slow purely gravitational collapse, and this scenario may underlie the observed clumpy high-z disks that appears to be in a violent kinematic state (Genzel et al. 2006). This more violent disk formation scenario is different from the likely formation process of the quiescent LSB galaxies in the nearby universe, which appear to have formed mostly from gravitational collapse alone. Despite the heterogeneity of the initial conditions, which allow some galaxies to by-pass certain stages of the evolution along the Hubble sequence, or else allow the galaxies to fast-evolve through the initial stages to build up a substantial bulge relatively early in time, the general trend of galaxy formation and evolution still appears to be through a disk-dominated configuration (van Dokkum et al. 2011). This is only reasonable because the large-scale gravitational instabilities which form spontaneously in disk galaxies can accelerate the speed of entropy evolution many orders of magnitudes higher compared to a smooth distribution (Zhang 1992), and nature, as it appears, has always chosen her evolution configuration that maximizes the entropy production rate. The support for this argument in a broader context is the theory on “dissipative structures” (Nicholis & Prigogine 1977): the large-scale coherent patterns present in nonlinear, far-from-equilibrium complex systems exist not merely as pretty and impressive veneers, they serve an important dynamical role of greatly accelerating the en-

tropy evolution of the underlying non-equilibrium system – in the case of a self-gravitating system, the direction of entropy evolution is towards configurations of ever-increasing central concentration, together with an extended outer envelope, and in the case of galaxies, this is the same direction as evolution along the Hubble sequence from late to early Hubble types.

It is for these reasons that we study the evolution of nearby galaxies along the Hubble sequence as a template for what could have possibly happened in galaxies in the more distant universe, even knowing that for individual galaxies the trend may not be all smooth and universal, i.e., the initial conditions may not all have been that of a thin disk, and the smooth disk-dominated evolution could be interrupted by a merger or satellite accretion. We also point out that the same phase-shift induced collective dissipation process is likely to operate in configurations that have a vertical extent as well: i.e., halos and the thick inner regions of galaxies may possess skewness which lead to the same kind of potential-density phase shift as in thin disks, and thus will have accelerated evolution according to the same basic dynamical process we describe for disk galaxies.

4 ANALYSES OF INDIVIDUAL GALAXIES

In this section, we analyze the morphology and kinematics of six bright, nearby galaxies, to set the stage for further evolutionary studies of these galaxies in the next section. The parameters of these six galaxies are given in Table 1. The total-mass maps derived using methods described below and in Appendix A are shown in Figure 2.

4.1 NGC 4321 (M100)

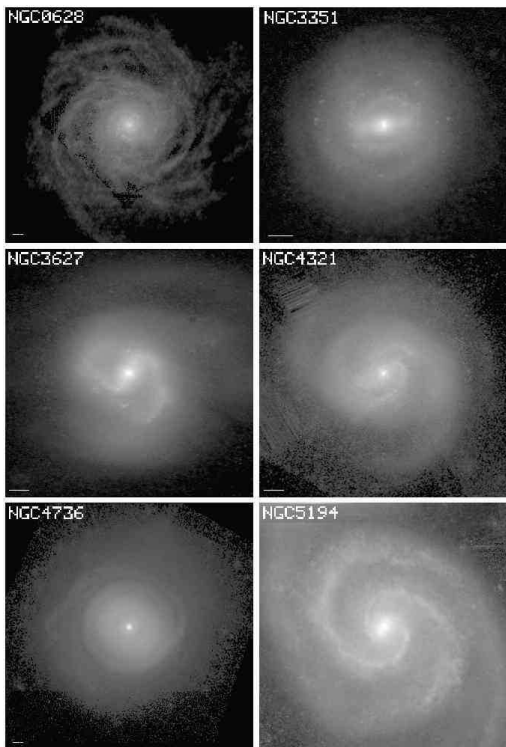
NGC 4321 (M100) is the bright Virgo spiral, of mid-infrared (MIR) RC3 type SAB(rs, nr)bc (Buta et al. 2010). It lies at a distance of approximately 16 Mpc. The procedure for calculating the surface density distributions for the stellar and gaseous components using the near- and mid-IR observations, as well as atomic and molecular interferometric observations of galaxies, is described in detail in Appendix A. Two stellar mass maps were derived, one based on a SINGS (Kennicutt et al. 2003) $3.6\mu\text{m}$ IRAC image, and the other based on a SDSS *i*-band image. The same HI and H_2 gas maps were added onto these stellar surface density maps to obtain the total disk surface density maps. The surface densities of the gaseous mass components alone, HI and H_2 , derived from VIVA (Chung et al. 2009) and BIMA SONG (Helfer et al. 2003), respectively, and the total mass profiles using the IRAC $3.6\mu\text{m}$ image and the SDSS *i*-band image (“tot 3.6 ” and “tot i ”, respectively), are illustrated in Figure 3. This shows that the $3.6\mu\text{m}$ and *i*-band total mass maps give very similar average surface density distributions for M100.

In ZB07 we carried out a phase shift analysis for this galaxy using the $3.6\mu\text{m}$ SINGS image, and assumed a constant mass to light ratio (M/L) without gas. Four sets of corotation (CR) resonances were found, and they were shown to correspond to well-defined morphological features. Figure 4, top, shows the radial-dependence of potential-density phase shift derived using the total stellar plus

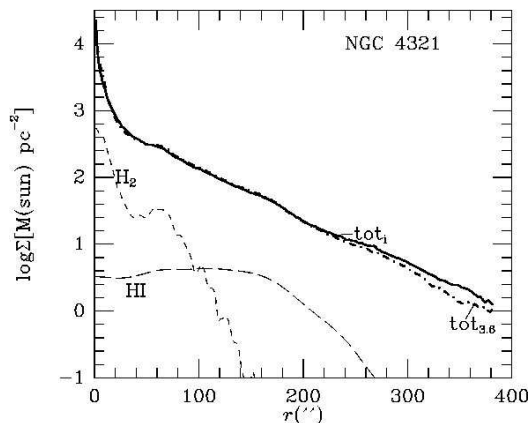
Table 1. Adopted parameters for sample galaxies.^a

Galaxy	i (degrees)	ϕ_n (degrees)	h_R (arcsec)	h_z (arcsec)	Distance (Mpc)	References for (i, ϕ_n)
NGC 628	6	25	64 (3.6)	7.1	8.2	Shostak et al. (1983)
NGC 3351	40.6	13.3	44 (3.6)	8.9	10.1	3.6 μm isophotes
NGC 3627	60	173	66 (3.6)	13.3	10.1	RC2, Zhang et al. (1993)
NGC 4321	31.7	153	63 (3.6)	12.6	16.1	Hernandez et al. (2005)
NGC 4736	30	116	135 (i)	27.1	5.0	3.6 $\mu\text{m}, g, i$ isophotes; Buta (1988)
NGC 5194	20 \pm 5	170 \pm 3	50 (K_s)	10.0	7.7	Tully (1974)

^aCol. 1: galaxy name; col. 2: adopted inclination; col. 3: adopted line of nodes position angle; col. 4: adopted radial scale length, not based on decomposition but from slope of azimuthally-averaged surface brightness profile (filter used in parentheses); col. 5: adopted vertical scale height derived as $h_z = h_R/5$ except for NGC 628 where $h_z = h_R/9$; col. 6: mean redshift-independent distance from NED; typical uncertainty $\pm 1\text{-}2\text{Mpc}$; col. 7: source of adopted orientation parameters.

**Figure 2.** Total mass maps of the six sample galaxies.

gaseous maps for the IRAC 3.6 μm band (left frame) and the SDSS i-band (right frame). We can see that these two maps give similar CR predictions (in terms of the positive-to-negative (P/N) zero crossings of the phase shift curves), except near the very center of the galaxy where the factor of 2 better spatial resolution of the SDSS map allows the resolving of a possible 4th pattern in the nuclear region. We have also tried to calculate phase shift distributions using images from the different optical and NIR wave bands that we have access to assuming constant M/L, and found that the phase shifts derived from the above total mass maps (calibrated with radial dependent M/L) show the best coherence, most likely due to the best kinematical and dynamical mutual consistency between the potential and density pair used for the total mass analysis, as is the case for physi-

**Figure 3.** Azimuthally-averaged surface mass density profiles of NGC 4321, based on the atomic (HI), molecular (H₂), and total (3.6 μm + HI + H₂ and i + HI + H₂) mass maps. The profile based on the 3.6 μm image is called tot_{3.6} while that based on the i -band is called tot _{i} .

cal galaxies. Table 2 lists the (unweighted) average CR radii from the 3.6 μm and i -band maps.

Figure 4, bottom shows the four CR circles for M100 superposed on the g -band SDSS image. The inset shows only the inner region, which in the g -band includes a nuclear pseudoring and in the longer wavelength bands includes a nuclear bar. The CR₁ radius determined from the new maps, (8. $^{\prime\prime}$ \pm 0. $^{\prime\prime}$ 7) is smaller than what we obtained previously (13. $^{\prime\prime}$) in ZB07, but turns out to better correspond to the features of the resolved inner bar. The nuclear bar seems to extend either a little beyond or just up to its CR and terminates in a broad, swept-up spiral section (a nuclear pseudoring) at the location indicated by the next N/P crossing. The next CR, CR₂, appears to be related to an inner spiral that breaks from near the nuclear pseudoring. The curved dust lanes in this spiral are on the leading sides of the weak bar. CR₃ appears to lie completely within the main spiral arms and could be the CR of the bar itself. The radius of CR₃, 52. $^{\prime\prime}$, is slightly less than that determined by ZB07, 59. $^{\prime\prime}$, and may lie a little inside the ends of the primary bar. CR₄, at 137. $^{\prime\prime}$, lies within the outer arms. These values should be compared with $r(\text{CR}) = 97.^{\prime\prime}\pm 15.^{\prime\prime}$ obtained by Hernandez et al. (2005) using the Tremaine-Weinberg method applied to an H α velocity field. Their value is close to the average of our CR₃ and CR₄ radii. We believe our two-outer-CR result is more reasonable than the single outer CR result from the

Table 2. Corotation radii from potential-density phase shifts

Galaxy	CR ₁ (arcsec)	CR ₂ (arcsec)	CR ₃ (arcsec)	CR ₄ (arcsec)	CR ₅ (arcsec)	Filters
NGC 628	7.4	39.2	81.5	253.0:	3.6
NGC 3351	26.2±0.4	86.5±5.1	3.6, <i>i</i>
NGC 3627	78.6±3.5	3.6, <i>i</i>
NGC 4321	8.3±0.7	28.8±0.6	51.9±0.0	136.9±1.6	3.6, <i>i</i>
NGC 4736	27	39	120	275	385	<i>i</i>
NGC 5194	21.3±3.1	110.1±0.1	3.6, <i>i</i>

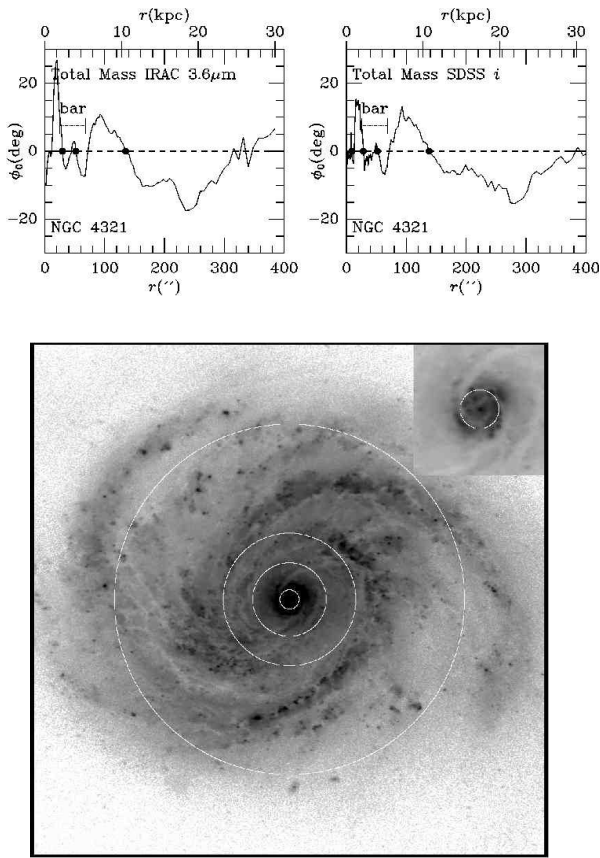


Figure 4. Top: Potential-density phase shift versus galactic radius for NGC 4321 derived using the total mass map with IRAC and SDSS data. CR radii are indicated by the filled circles. The radius range of the bar from ZB07 is indicated. Bottom: Corotation circles overlaid on a deprojected SDSS *g*-band image of NGC 4321. The main frame covers an area 6'.4 square, while the inset is 0'.8 square. The units are mag arcsec⁻².

TW method for this galaxy, because on the *g*-band overlay image one can clearly discern the dust lanes moving from the inner/leading edge of the spiral to outer/trailing edge across CR₄, indicating the location where the angular speed of disk matter and density wave switch their relative magnitude. CR₃ on the other hand is tied to the main bar rather than the spiral.

It appears that the patterns surrounding CR₁ and CR₃ are best described as super-fast bars (ZB07, BZ09) of a dumb-bell shape with their thick ends created by the different pattern speeds interacting in the region of their encounter (see also the classification in Appendix B). Super-

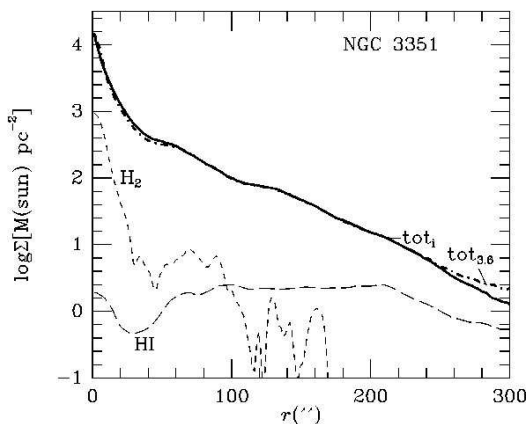


Figure 5. Azimuthally-averaged surface mass density profiles of NGC 3351. The layout is the same as in Figure 3.

fast bars are a peculiar implication of the phase shift method, because they contradict the results of passive orbit analyses that imply that a bar cannot extend beyond its own CR due to a lack of orbital support (Contopoulos 1980).

4.2 NGC 3351 (M95)

NGC 3351 (M95) is a barred spiral galaxy of MIR RC3 type (R')SB(r, nr)a (Buta et al. 2010). It lies at a distance of approximately 10 Mpc. The surface densities of the different mass components for this galaxy derived using IRAC, SDSS, BIMA SONG and THINGS data are shown in Figure 5. Phase shift analyses for NGC 3351 were carried out using the IRAC and SDSS mass surface density images based on the 3.6 μ m SINGS and *i*-band SDSS images, plus the gas maps (Figure 6, top). The phase shift distributions for both the IRAC and SDSS total mass maps show a major CR near $r = 86''$, and also another CR at $r = 26''$.

Figure 6, bottom shows the two CR radii as solid circles superposed on the *g*-band image. Two prominent N/P crossings follow these CR radii at 65'' and 128''. For comparison, the inner ring of NGC 3351 has dimensions of 71''.0 × 67''.8 and lies close to the first N/P crossing, implying that the ring/spiral is a separate mode whose CR is CR₂ at 86''. In Figure 6, top also, the extent of the main part of the bar is indicated, and both mass maps show the same thing: the phase shifts are negative across the main part of the bar, implying (as discussed in ZB07 and BZ09) that the corotation radius of the bar is CR₁, not CR₂. Thus, NGC 3351 is also a case of a super-fast bar.

The inner pseudoring at the location of the first major N/P crossing would, in passive orbit analysis in a galaxy

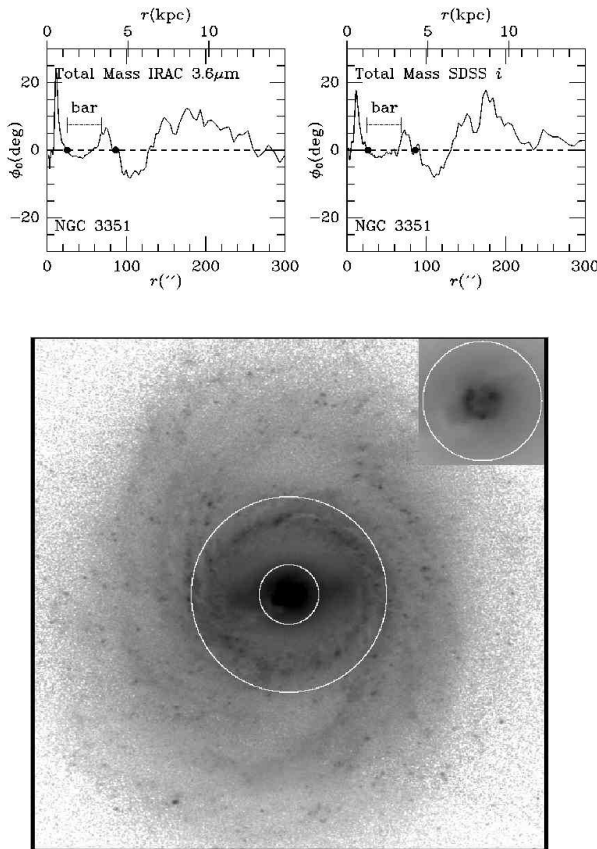


Figure 6. *Top:* Potential-density phase shift versus galactic radius for galaxy NGC 3351 derived using the total mass map with IRAC and SDSS data. *Bottom:* Deprojected *g*-band image of NGC 3351 in units of mag arcsec⁻², with major phase shift crossings superposed as solid circles. The main frame covers an area 7.5' square, while the inset is 0.93' square.

with a bar and non-self-gravitating clouds, be considered an inner 4:1 resonance ring as identified by Schwarz (1984) and Buta & Combes (1996). This ring would be directly related to the bar and have the same pattern speed as the bar. Our phase shift analysis, however, suggests that the apparent ring/pseudoring could be due to a “snow plough” effect of two sets of inner/outer patterns having different pattern speeds, and which thus accumulate mass at that radius. The strong and symmetric arms which end a little within the second CR circle might be related to what Patsis/Contopoulos/Grosbol had advocated: that symmetric patterns sometimes end at the inner 4:1 resonance (counter-examples are discussed by ZB07 and BZ09). The spiral patterns outside the second CR circle in this case are more fragmented. It is not yet clear what different dynamics would make some spirals extend all the way to OLR and others end mostly within CR or inner 4:1. Perhaps those that have CRs intersecting the arms (such as NGC 5247 analyzed in ZB07) tend to be Sb, Sc or later types, such that the arms are going through the transitional phase from a skewed long inner bar to either a bar-driven spiral or an inner organized spiral plus outer diffused arms. Therefore, the ones where the spiral ends at the inner 4:1 resonance or CR (i.e. the NGC 3351 type) should tend to be more mature and more

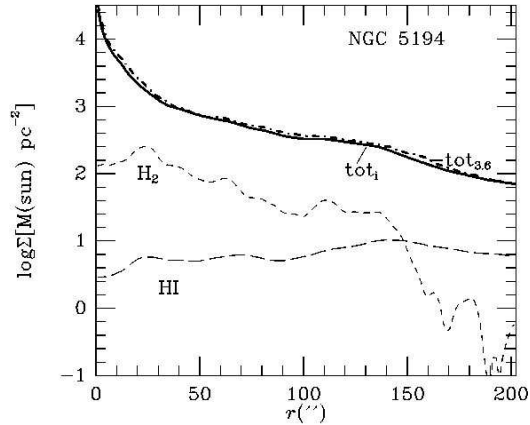


Figure 7. Azimuthally-averaged surface mass density profiles of NGC 5194. The layout is the same as in Figure 3.

steady types, i.e., earlier-type disks in general than those with arms being crossed by the CR circle.

4.3 NGC 5194 (M51)

NGC 5194 (M51) is the proto-typical interacting grand design spiral, of MIR RC3 type SAB(rs, nr)bc (Buta et al. 2010). It lies at a distance of approximately 8.4 Mpc. The surface densities of the different mass components for this galaxy derived using IRAC, SDSS, BIMA SONG and THINGS data are shown in Figure 7. It can be seen that the hot dust-corrected total 3.6 μ m surface density profile and that for the *i*-band data are very similar.

The potential-density phase shift method was used to derive the main CR radii for this galaxy (Figure 8). By focusing on the area that just excludes the small companion NGC 5195, which is likely to lie outside of the M51 galactic plane and thus have minor influence on the internal dynamics of M51 at the epoch of observation (a conjecture which is confirmed by our analysis), the phase shift analysis gives two major CR radii (P/N crossings on the phase shift plot, represented by solid circles on the overlay image) followed by two negative-to-positive (N/P) crossing radii (not shown on the overly). The latter are believed to be where the inner modes decouple from the outer modes. The CR radii, at 21'' \pm 3'' and 110''. (Table 2), match very well the galaxy morphological features [i.e., the inner CR circle lies near the end of an inner bar/oval, and the first N/P crossing circle ($r=30''$) is where the two modes decouple]. Also, for the outer mode, the CR circle seems to just bisect the regions where the star-formation clumps are either concentrated on the inner edge of the arm, or on the outer edge of the arm – a strong indication that this second CR is located right near where the pattern speed of the wave and the angular speed of the stars match each other (this can be compared to a similar transition of arm morphology across CR in the simulated galaxy image of Z96 Fig 3). This supports the hypothesis that the spiral patterns in this galaxy are intrinsic modes rather than tidal and transient, and that tidal perturbation serves to enhance the prominence of the intrinsic mode, but does not alter its modal shape.

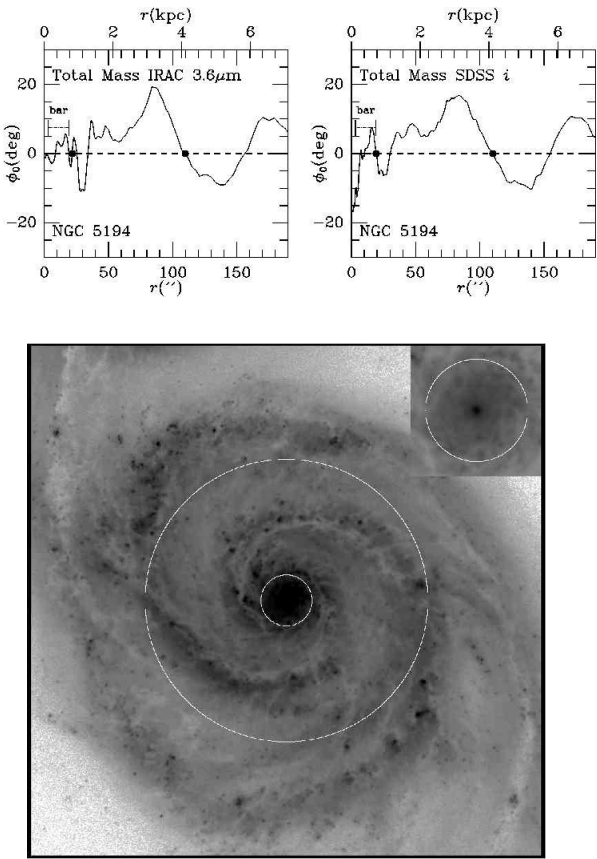


Figure 8. Top: Calculated phase shift vs galaxy radii for NGC 5194 (M51) using the IRAC data as well as SDSS data. Two corotation radii (filled circles) are indicated. Bottom: CR circles overlaid on the deprojected g -band image of NGC 5194 (M51). The main frame covers an area $6'6$ square, while the inset is $0'93$ square. The units are mag arcsec $^{-2}$.

4.4 NGC 3627 (M66)

The intermediate-type barred spiral galaxy NGC 3627, of MIR RC3 type SB(s)b pec (Buta et al. 2010), is a member of the interacting group the Leo Triplet (the other two members being NGC 3628 and NGC 3623). It lies at a distance of approximately 10 Mpc. The surface densities of the different mass components for this galaxy derived using IRAC, SDSS, BIMA SONG and THINGS data are shown in Figure 9. As for NGC 3351, 4321, and 5194, the total $3.6\mu\text{m}$ mass profile and the total i -band mass profile are in good agreement over a wide range of radius.

Zhang, Wright, and Alexander (1993) observed this galaxy in high-resolution CO(1-0) and HI, and found that the choice of an outer CR location at $220''$ coinciding with the outer HI cutoff could account for many observed morphological features. Subsequent observations, e.g. those of Chemin et al. (2003) in the $\text{H}\alpha$ line has determined that that an inner CR enclosing the central bar is a more reasonable choice. In the following, we use the new surface density maps to re-evaluate the question of CR determination for this galaxy, bearing in mind however that the potential-density phase shift method we use in the current study will give the most reliable CR determination for potential-density pairs that have achieved dynamical equilibrium, a condition which

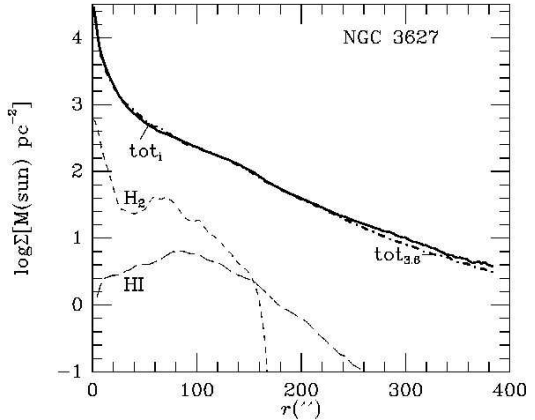


Figure 9. Azimuthally-averaged surface mass density profiles of NGC 3627. The layout is the same as in Figure 3.

is likely to be violated for this strongly-interacting galaxy that has suffered serious damage in its outer disk (Zhang et al. 1993).

In Figure 10, top, we show the phase shifts with respect to the total potential of the total mass distribution, as well as for the total gas distribution. The total mass phase shifts displays only one inner CR at $78''6 \pm 3''5$, which can be compared to the CR radius obtained by Chemin et al. (2003) of $\sim 70''$, yet the large-radius phase distribution shows clear evidence of the disturbance caused by the interaction, and thus (by implication) a lack of dynamical equilibrium. The main CR appears to encircle the bar ends in NGC 3627 (Figure 10, bottom), which would make the galaxy a “fast bar” case according to BZ09 (see also Appendix B).

The total gas phase shift shows the presence of a second possible CR between $220''$ - $260''$, close to the one adopted in Zhang et al. (1993) of $220''$. The radius of this possible CR is ill-defined since the phase shift barely reaches zero and does not become a clear P/N crossing. Figure 10, bottom, shows the g -band image overlaid with the two possible CR circles, selecting $220''$ for the outer CR as the minimum likely value. The total mass map shows two faint outer arms that extend towards the outer CR circle – in fact these outer spiral arms extend much further than the impression given in the g -band image, as can be seen in the non-deprojected HI surface density profile (Zhang et al. 1993, Figure 7; as well as a similar HI image in the THINGS website).

According to the one-CR view of Chemin et al. (2003), the main spiral would be bar-driven. However, this view would be contradicted by the two strong disconnected bow-shocks at the CR circle, indicating the interaction of two pattern speeds (these disconnected bow shock segments in fact show up more clearly in the gas surface density map). Truly bar-driven spirals do not contain these disconnected bow-shock segments and the spirals would appear as the further continuation of a skewed bar (see Appendix B). The outer spiral arms in the case of NGC 3627 clearly do not connect smoothly with the inner bar – in fact, there is evidence of two sets of spiral patterns, the inner set with short arms appears bar-driven whereas the outer set is offset in phase in the azimuthal direction from the inner one.

With this additional evidence, we propose that prior to the encounter with NGC 3628, NGC 3627 originally had a

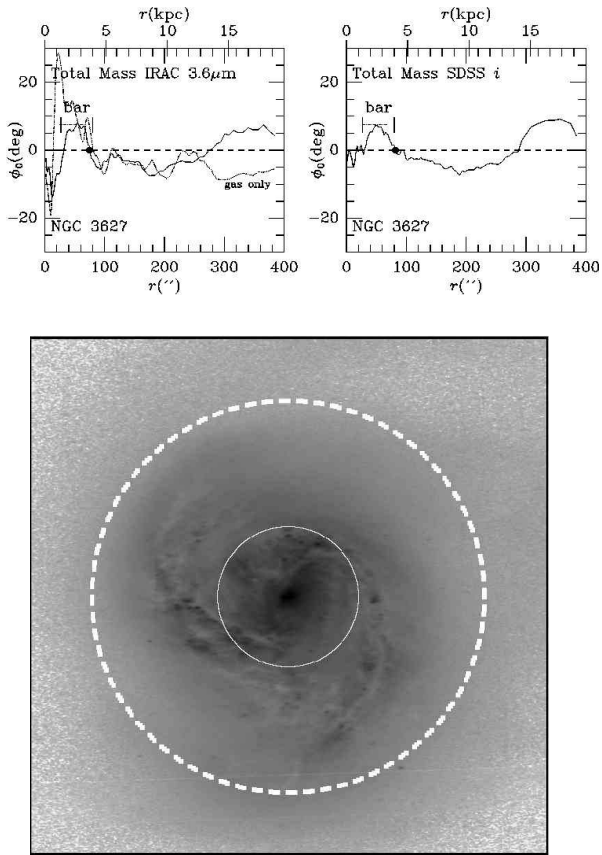


Figure 10. Top: Calculated phase shifts between the stellar mass and total potential, and the HI gas mass and the total potential, for NGC 3627. Bottom: Overlay of CR circles on the *g*-band image for NGC 3627. The main frame covers an area 9.6 square. The units are mag arcsec⁻².

two-pattern structure similar to the CR3 and CR4 regions of NGC 4321. The interaction tore out a large part of the outer surface density from NGC 3627, including a segment of the outer spiral arm (Zhang et al. 1993, Figure 5, clump L). Therefore the galaxy is evolving towards a new dynamical equilibrium, with the possibility of losing the coherent outer spiral pattern eventually.

4.5 NGC 628

NGC 628 is a late-type spiral of MIR RC3 type SA(s)c (Buta et al. 2010). It lies at a distance of 8.2 Mpc. The surface densities of the different mass components for this galaxy derived using IRAC, BIMA SONG and THINGS data are shown in Figure 11. For this galaxy, no SDSS data are available. Unlike the other galaxies in our sample, NGC 628 has considerable HI gas at large radii, and this accounts for the significant departure of the total mass profile from the stellar density profile alone.

The phase shift plot (Figure 12, top) shows noisier organization compared to all the other galaxies in this sample, which is consistent with this galaxy being of very late type. In the secular evolution picture this corresponds to a young galaxy still in the process of settling down towards a dynamical equilibrium state. Nevertheless, there is an in-

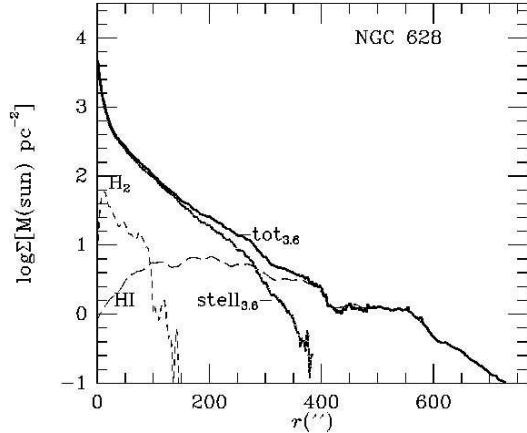
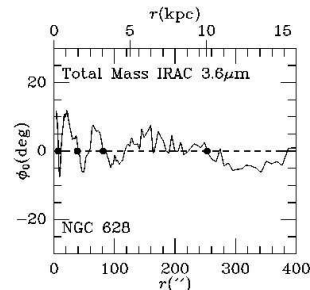


Figure 11. Azimuthally-averaged surface mass density profiles of NGC 628. The HI and H₂ profiles are shown, and the stellar and total mass profiles based on a 3.6μm image.



dication of four P/N crossings which are indicated by the filled circles in the figure. Table 2 lists the radii of these crossings. Figure 12, bottom shows the overlay of CR circles on a deprojected *B*-band image of NGC 628.

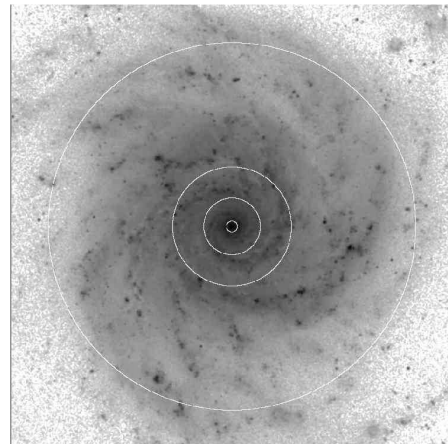


Figure 12. Top: Phase shift between the total mass surface density and total potential for NGC 628. Bottom: Deprojected *B*-band image of NGC 628 overlaid with CR circles. The main frame covers an area 10.1 square. The units are mag arcsec⁻².

dication of four P/N crossings which are indicated by the filled circles in the figure. Table 2 lists the radii of these crossings. Figure 12, bottom shows the overlay of CR circles on a deprojected *B*-band image of NGC 628.

4.6 NGC 4736

NGC 4736 is an early-type spiral of MIR RC3 type (R)SAB(rl,nr',nl,nb)a (Buta et al. 2010), implying a galaxy

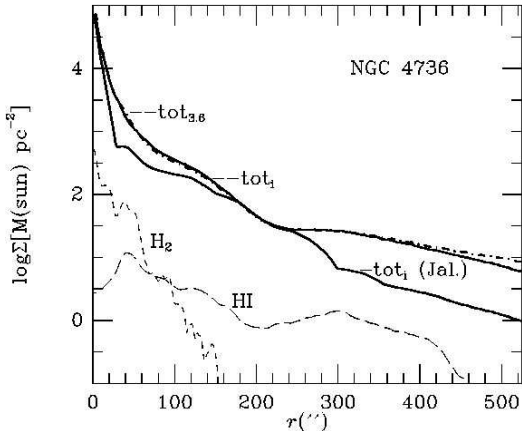


Figure 13. Azimuthally-averaged surface mass density profiles of NGC 4736. The layout is the same as in Figure 3, except that graph includes the profile scaled according to the mass-to-light ratio profile used by Jalocha et al. (2008).

with many distinct features. It lies at a distance of about 5 Mpc. For the derivation of the stellar mass map, we have used the SDSS *i*-band data and the mass-to-light profiles obtained through a fitting procedure by Jalocha et al. (2008). This is because the usual color-based approach (Bell & de Jong 2001) gives a stellar surface density distribution that leads to a predicted rotation curve much higher than the observed rotation curve in the central region of the galaxy. We have not made further correction to account for the fact that Jalocha et al. used the Cousins *I*-band data whereas we are using the SDSS *i*-band data, since we expect the uncertainties in the M/L determination would be larger than these differences. The surface mass density curves for this galaxy are shown in Figure 13. The tot_{3.6} and tot_{*i*} curves were derived in the same manner as for the other galaxies. The tot_{*i*} (Jal.) is based on the purely radius-dependent *M/L* from Jalocha et al. (2008).

The phase shift derived using the total mass map and the overlay of CR circles on the image is given in Figure 14. The shift plot (Figure 14, top) shows several well-delineated P/N crossings (Table 2) which appear to correspond well to the resonant structures in the image (Figure 14, bottom). CR₁ could be associated with an inner nuclear bar, while CR₂ is a mode associated with the bright spiral inner pseudoring. CR₃ could be associated with an intermediate spiral pattern outside the prominent inner ring. The fact that CR₄ passes through the gap between the inner and outer rings suggests that it is the actual CR of the massive oval. CR₅ may be associated with the outer ring pattern.

5 ANALYSES OF THE SAMPLE, AND DISCUSSION

5.1 Rotation Curves, Secular Mass Flow Rates, and Their Implications on the Compositions of Galactic Dark Matter

In the next group of figures (Figure 15 and Figure 16), we present the rotation curves (observed, versus disk-total-mass-derived) as well as the total mass flow rates for our sample galaxies. The sequence of arrangement for the differ-

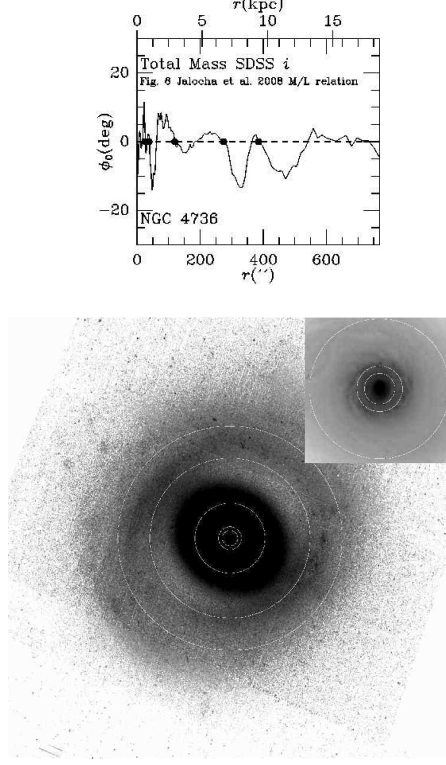


Figure 14. Top: Phase shift between the total mass surface density and total potential for NGC 4736, derived using the SDSS data. Bottom: SDSS *g*-band image of NGC 4736 with the CR circle overlay. The main frame covers an area 25'4 square, while the inset has an area 4'25 square. The units are mag arcsec⁻².

ent frames, NGC 0628, NGC 4321, NGC 5194, NGC 3627, NGC 3351, NGC 4736, from left to right, then top to bottom, is chosen to be roughly along the Hubble diagram from the late to the early types, in order to reveal any systematic trends along this sequence. Notice, however, that two of the intermediate types (NGC 5194 and NGC 3627) are strongly interacting galaxies, and thus they might deviate from the quiescent evolution trends. Note also that since there is usually a limited radial range for the availability of observed rotation curves, our subsequent plots in this section (Figures 15-21) will be displayed with a smaller radial range than their corresponding phase shift plots in the last section.

The sources of the observed rotation curves are as follows: N0628: from Nicol (2006)'s SINGS sample follow-up H-alpha observations. N4321: From the CO/H-alpha compiled rotation curve of Sofue et al. (1999). N5194: From Sofue (1996) compiled rotation curve. N3627: Inner part from Zhang et al. (1993)'s CO 1-0 observation (rescaled to the current distance value, and changed to use terminal velocity instead of peak velocity of the molecular contours), outer part from Chemin et al. (2003)'s H-alpha observation. N3351: Inner part from Devereux, Kenney, & Young (1992)'s CO 1-0 observation, outer part from Buta (1988) H-alpha observation. N4736: From Jalocha et al. (2008), which was adapted from Sofue et al. (1999) compilation. From Figure 15, we observe that the contribution of the disk baryonic matter (ex-

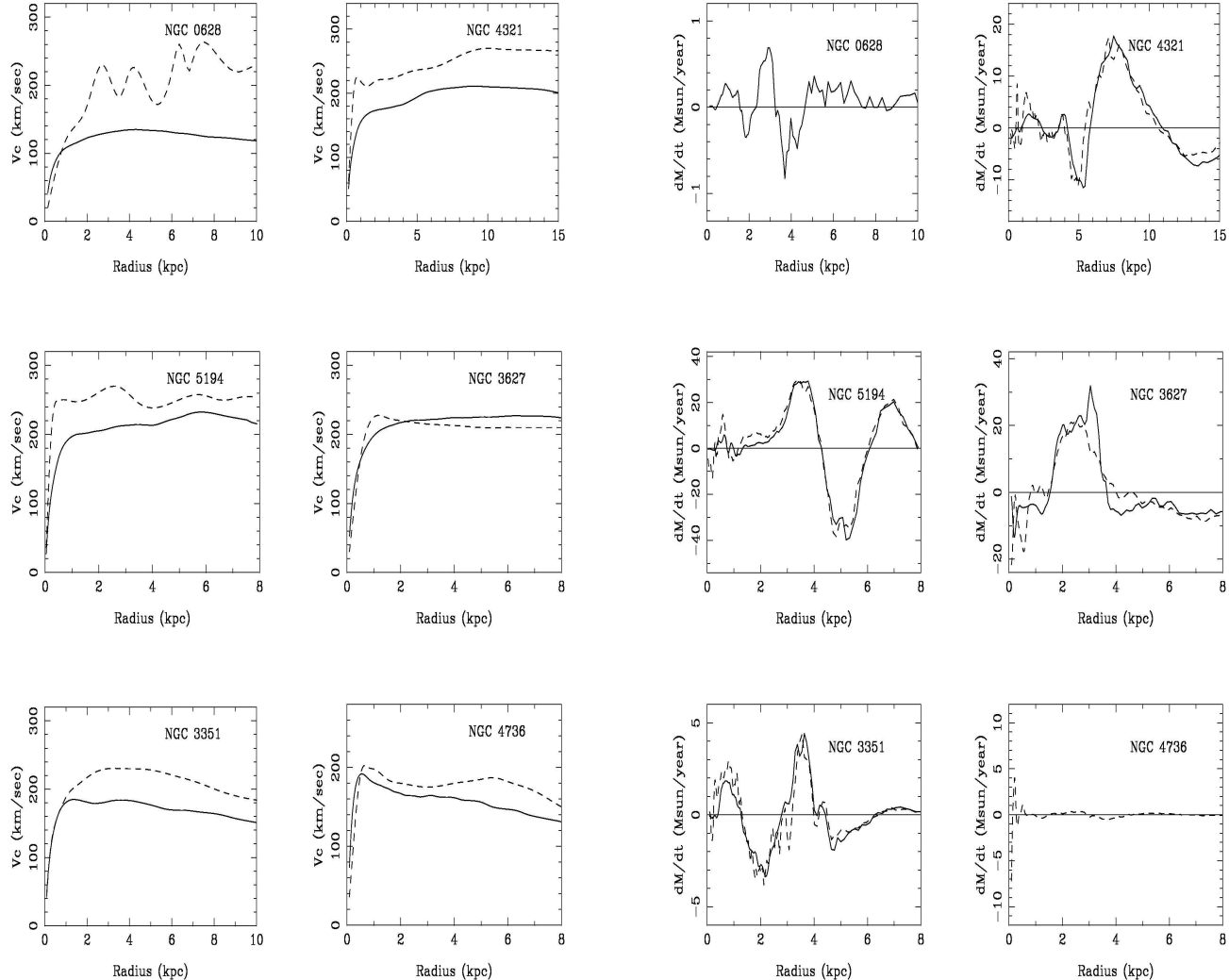


Figure 15. Comparison of rotation curves for the six sample galaxies. Solid lines: Disk rotation curves inferred from total disk surface density (stellar plus atomic and molecular hydrogen mass). Note that very small correction to account for helium and metal abundance in the gas mass has not been made). The inferred disk rotation curves were derived using IRAC 3.6 μm data for NGC 0628, using an average of IRAC 3.6 μm and SDSS i-band data for NGC 4321, 3351, 3627, 5194, and using SDSS i-band data for NGC 4736, plus the atomic and molecular gas contribution from the VIVA, THINGS and BIMA SONG observations. Dashed lines: Observed rotation curves. The sources for these observations are given in the main text.

cluding the contribution from Helium and heavy elements) to the total rotation curve increases as the galaxy's Hubble type changes from the late to the early as the galaxy evolves along the Hubble sequence. For early-type galaxies such as NGC 4736, the entire rotation curve may be accounted for by disk baryonic matter (Jalocha et al. 2008). Note that the close match between the observed and disk-inferred rotation curves for NGC 3627, which is unusual because of its intermediate Hubble type, maybe be a result of the close en-

Figure 16. Total radial mass flow rate for the six sample galaxies. Positive portion of the curves indicate inflow, and negative portion of the curves indicate outflow. The solid lines have stellar mass derived from IRAC 3.6 μm data, and the dashed lines have stellar mass derived from SDSS i-band data. Atomic and molecular gas mass from VIVA, THINGS and BIMA SONG were added to obtain the total mass maps which were used to derive these flow rates.

counter with NGC 3628 which likely to have striped a large portion of its halo.

We have verified that the mass flow rates calculated according to the prescriptions in §2 is not sensitively dependent on the choice of scale height in the potential calculation (i.e. a change of Hz from 12.6" to 3.8" in the case of NGC 4321 changed the scale of mass flow by only 10% or less for the entire radial range considered). From Figure 16, we see that the mass flow rates for the various Hubble types range from a few solar masses per year to about a few tens of solar masses a year, except for the very late type galaxy NGC 628 which is still in the process of coordinating a significant galaxy-wide mass flow pattern. The intermediate-type galaxies appear to have the largest mass flow rates

(the one galaxy, NGC 1530 studied in ZB07, which has mass flow rates on the order of 100 solar mass a year, is also an intermediate-type galaxy), whereas for the early-type galaxies the mass flow is more concentrated to the central region. Although both inflow and outflow of mass are present at a given instant across a galaxy's radial range, due to the need to support the structure of density wave modes which have alternating positive and negative angular momentum density outside and inside CR, respectively (this inflow and outflow of mass for a density wave mode was also previously confirmed in the N-body simulations of DT94 and Z96), there is a general trend for the mass to concentrate into the inner disk with time, together with the build-up of an extended outer envelope, consistent with the direction of entropy evolution. This trend will be confirmed next in Figure 17, which shows that for late and intermediate-type galaxies the gravitational torque couple (and so is advective torque couple which has similar shape) has mostly positive values in the inner disk, which shows that the angular momentum is consistently being channeled out of the galaxy. There is also a trend there that the mass flow and angular momentum channeling activity progressively moves from the outer disk to the inner disk as a galaxy evolves from the late to the early Hubble types.

Note that the radial mass flow rates presented in these curves are actually the lower bounds on the actual radial mass flow rates due to nonaxisymmetric instabilities in physical galaxies, since these instabilities are expected to result in skewed distributions in parts of the thick-disk and halo as well, and thus result in the radial redistribution of the halo dark matter along with the luminous disk matter (with the composition of the dark component likely to be made of baryons too, see discussions that follow). The nonaxisymmetric instabilities in the spheroidal components are reflected in the twisted isophotes often observed in disk elliptical galaxies. These twisted distributions in the spheroidal components will lead to the same potential-density phase shift and collective secular mass redistribution as we discussed for the disk component. Therefore, the average mass flow rate is sufficient for the build-up of Milky Way type Bulge in a Hubble type, and for some of the strongly interacting or else high-wave-amplitude isolated galaxies (like NGC 1530), evolution towards disk ellipticals within a Hubble time is also entirely possible.

This picture of the gradual build-up of the Hubble sequence by the radial accretion of the baryonic matter, however, poses a significant challenge to the currently popular LCDM paradigm: The magnitudes of the mass flow rates appear large enough to be able to effect a significant Hubble type transformation during the past Hubble time (i.e. 10 solar masses a year corresponds to 10^{11} solar mass during the past 10^{10} years, enough to build up a massive central bulge in a Milky-Way type galaxy). The mass flow rates are especially large for galaxies experiencing strong tidal perturbations (i.e. NGC 3627 and NGC 5194), due to the large-amplitude density wave patterns excited during these strong interactions. The interaction-enhanced secular evolution effect can thus underlie the well known morphological Butcher-Oemler effect in clusters (Butcher & Oemler 1978) which transform late type disks to early-type spirals and S0s. The effect is also likely responsible for producing

the morphology-density relation in different galaxy environments (Dressler 1980).

If the galaxy rotation curve (RC) and mass flow rates indicate that along the Hubble sequence from late to early, more and more of the RC is contributed by luminous baryonic matter as a result of secular mass accretion, then where did the non-baryonic cold dark matter (CDM) go as this evolution proceeds? The CDM could not simply be displaced by the baryonic matter, since a well-known result of the LCDM numerical simulations is the so-called adiabatic compression of the dark matter halos (see, e.g. Sellwood & McGaugh 2005 and the references therein), i.e. as the baryons become more centrally-concentrated, the dark matter particles should be dragged into the central potential wells thus formed, since the dark matter particles are cold as hypothesized.

To resolve this paradox, in fact the most natural solution is to hypothesize that the galactic dark matter is mostly made of dark baryons. This baryonic dark matter could be in the form of brown dwarfs and other non-luminous Massive Compact Halo Objects (MACHOs) as revealed by microlensing observations (Alcock et al. 1997; Koopmans & De Bruyn 2000). Some may argue that the current microlensing surveys have not uncovered enough dark matter to account for all that is needed to reproduce the galactic rotation curve, and that the extrapolated initial mass function (IMF) for star formation in the galactic plane does not seem to produce enough mass to close the gap either. We comment that the current microlensing observations may still be incomplete, and part of the discrepancy from the IMF argument may be due to the fact that IMF in different environments may be significantly different (i.e., in the disk plane the star formation is caused by spiral density wave shocks, and thus produce a family of stars that weigh heavily towards high mass stars. The mass formed in the quiescent environment of the halo and outer galaxy may on the other hand weigh heavily towards low mass stars and sub-stellar objects.

This proposal for the form of galactic dark matter not only makes the secular evolution picture more consistent (since the brown dwarfs have smaller mass, they can be displaced to the outer galaxy as the galaxy establishes new dynamical equilibrium – this is a kind of diffusion or dynamical friction effect), but it also makes other known paradoxes in the LCDM paradigm, such as the core-cusp controversy of the LSB and dwarf galaxies (de Blok 2010), as well as the difficulty of forming galaxies with realistic rotation curves in the LCDM simulations whenever the baryonic matter fraction is not high enough (White 2009), be easily solved. This solution would make the Hubble sequence galaxy dynamics all the more transparent: The early-type galaxies have cuspy mass distribution because the baryons there are more concentrated through secular evolution. In certain early-galaxies, such as NGC 4736, it has been found that the contribution of dark matter to the total mass distribution is very small (Jalocha et al. 2008). The late-type galaxies, on the other hand, are dark-matter dominated but were often found to have core-shaped mass distribution contrary to the LCDM prediction. In our current picture this can be understood easily since in late-type galaxies secular evolution has just been launched, and not enough central flowing of matter has been accomplished. The secular evolution scenario can naturally account for many other observed regularities of galactic structure and kinematics along the

Hubble sequence, such as the galaxy scaling relations and the existence of a Universal Rotation Curve trend (Zhang 2004, 2008), which were previously difficult to account for in the LCDM framework.

It is a well-known fact that a fraction of the baryonic matter has to be dark, from the discrepancy between the predicted cosmic baryon fraction through Big Bang nucleosynthesis, and the local observed values (Persic and Salucci 1992; Fukugita, Hogan, & Peebles 1998; McGaugh et al. 1010). If a fraction of the baryons can be dark, then more of it potentially can be dark as well. This proposal for the composition of dark matter to be made of mostly dark baryons works well for many known dark matter observations such as the colliding Bullet Cluster (Clowe et al. 2006) and the Train-Wreck Cluster (Mahdavi et al. 2007), which are sometimes difficult to reconcile under the standard LCDM paradigm (i.e. in the Bullet Cluster this dark matter seems to cluster with the stars in the outer two humps and not with the gas that is in the middle of the collision remnant, and yet in the Train-Wreck cluster the dark matter clusters with both the stars in the outer two humps as well as the central gas clump). In our new picture, since the baryonic dark matter consisting of MACHO-type objects that have a mass spectrum that can go from sub-stellar objects all the way to dust particles, it can display a more or less degree of dissipation as its detailed composition entails. In the Bullet cluster, the mass spectrum of the baryonic dark matter probably lean more towards slightly sub-stellar, whereas in the Train-Wreck cluster a more continuous spectrum from the barely sub-stellar to the super-dusty were all present, and the collision dynamics serves as a graded sieve to separate and arrange these mass components along a continuous path.

This proposal also easily eliminated the frustration of the non-detection of CDM particles, as well as some obvious challenging consequences we have to face if the CDM particles are in our midst. If the CDM particles gravitationally cluster with the baryons as hypothesized, and are mixed with the baryons in a ratio of 5 to 1, how come we could not feel their presence and detect their dynamical consequences say in the earth's atmosphere, which is gravitationally bound to the earth itself. And the increasingly-strong evidence of the down-sizing trend for structure formation (Cimatti et al. 2006; Nelan et al. 2005) is another serious challenge to the bottom-up mass assembly scenario of the LCDM paradigm, and the same trend is much more easily understood in the secular evolution picture.

We comment here also that our preference for MACHOs as candidates for a significant fraction of the galactic dark matter, as opposed to exotic forms of non-luminous gaseous baryons that reside in the galaxy disk (e.g. Pfenniger & Combes 1994), is due first of all, to the trend of properties seen along the Hubble sequence, i.e. the late-type disk galaxies have the highest dark matter contribution to their RCs, and yet their (luminous) disks are the lightest. Therefore, if the hypothesized non-luminous disk-gas baryons come in fixed fraction with the luminous disk-gas baryons, this trend of spheroidal-to-disk mass ratio along the Hubble sequence would be hard to account for. Secondly, from the modal theory of Bertin et al. (1989), density wave morphology along the Hubble sequence is linked to a galaxy's basic state properties. The fact that late-type galaxies have open and multi-

armed spiral patterns require that their parent basic state is such that most of the dynamical mass resides in a spherical halo, which is naturally consistent with the the dark matter being a MACHO type of halo dark matter, and is inconsistent with it being cold and non-luminous disk gaseous matter.

The unlikelihood of the galactic dark matter being made of hot gas, on the other hand, is due to the fact that hot gas usually has a very diffused and extended distribution, and its role is very minor in the secular transformation of Hubble types which requires mass to be accreted into the central region of a galaxy on the time scale of a fraction of a Hubble time. Hot gas will first need to dissipate its energy and settle onto the disk for it to participate in the global-instability-facilitated secular evolution, and even after that it is a long way from the outer galaxy to the central region. Even with the facilitation of disk global instabilities, we know the secular orbital decay rate is only a few kpc per Hubble time (Z99).

The observations of the Bullet Cluster are also inconsistent with the dark matter being made of a mostly dissipative gas component (either cold or hot gas).

This choice on the nature of galactic dark matter does leave us with the demanding task of rethinking the cosmic evolution history given by the concordance LCDM cosmological model. But, it is a reasonable assumption that we are in better understanding of local physics than we are of the distant universe, and the uncertainties in the details of the models of the universe certainly do not exclude the possibility of baryons as the major contributor of the dark matter (for example, a slight variation with time of the fundamental constants, such as the gravitational constant G, could lead to a different prediction on the expansion rate in the early universe, and thus different predictions on the results of primordial nucleosynthesis that would make it possible to accommodate a larger present-day baryon fraction; Likewise, the relative strengths of the different peaks on the CMB angular spectrum are not uniquely fitted by the current concordance parameter set – and it is well known that the acoustic peaks in the CMB angular spectrum were first predicted in purely baryonic cosmological theories [Sakharov 1965, Sunyaev & Zeldovich 1969; Peebles & Yu 1970]). And the local physics, as revealed by observations of the physical properties of galaxies and by the secular evolution scenario for galaxy morphological transformation, seems to strongly suggest that our current fundamental cosmological theories about structure formation is in need of major revision.

5.2 Relative Contributions from Gravitational and Advective Torque Couples, and Relations to Other Studies of Symmetry Breaking and Collective Effects

In Figure 17, we plot the calculated gravitational torque couple for the six sample galaxies. First we discuss the result for NGC 4321. This torque result is very similar in shape to the one calculated for the same galaxy by Gnedin et al. (1995), though the scale factor is more than a factor of 10 smaller than obtained in their paper. Part of the difference can be accounted for from the difference in galaxy images and in the galaxy parameters used between these two studies. We have tried to switch to use an R-band image as in Gnedin et

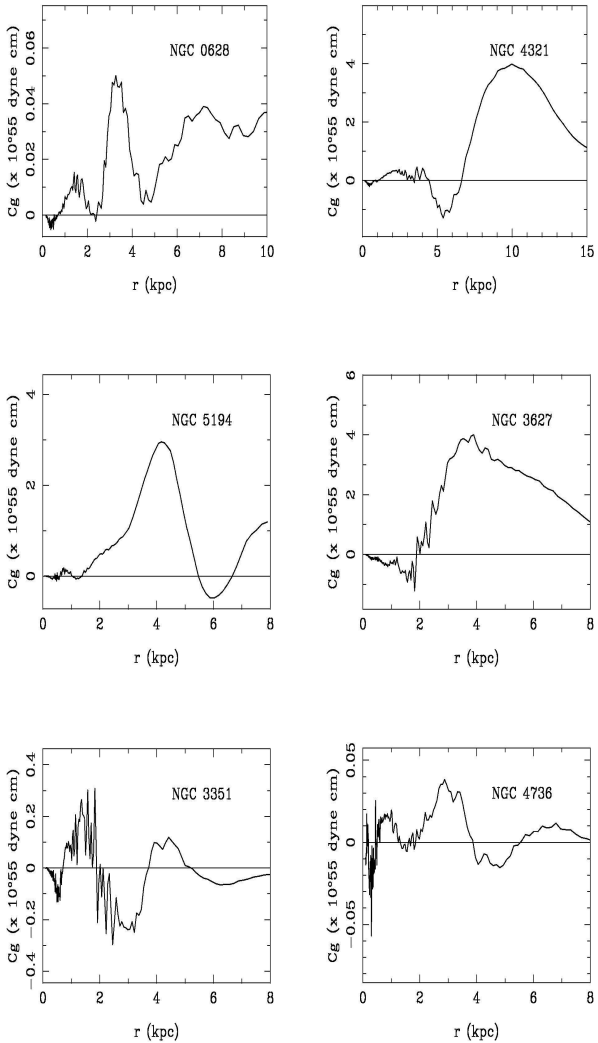


Figure 17. Calculated gravitational torque coupling for the six sample galaxies, using IRAC 3.6 μm data for NGC 0628, an average of IRAC 3.6 μm and SDSS i-band data for NGC 4321, 3351, 5194, 3627, and SDSS i-band data for NGC 4736, to these the usual gas maps were added.

al., and rescaled the galaxy parameters to be in agreement with what they used. However, after these adjustments the resulting scale is still smaller by a factor of ~ 5 from that in the Gnedin et al. (1995). The same amount of magnitude difference is recently found by Foyle et al. (2010) as well when they try to reproduce the Gnedin et al. result. It is possible that there was an internal error in the Gnedin et al. calculation.

As we see from a close inspection of Figure 17, for most of the galaxies in the sample, especially those of late to intermediate Hubble types, there is a main peak of the gravitational torque couple, which is centered in the mid disk. Thus the implied mass inflow/outflow should be focused around the mid disk near the peak location of the main bell curve. This location, however, is expected to change with time for a given galaxy as secular evolution proceeds, since the basic state configuration and the resulting modal configuration will both evolve due to the redistribution of the disk mass.

In fact, by examining this small sample of six galaxies, we can already see a trend that the main peak of the C_g curve moves from the outer region of the galaxy (as for NGC 0628) to the mid-disk (as for NGC 4321, 5194 and 3627), and then onward to the central region (NGC 3351 and 4736).

The existence of the multiple humps of the gravitational torque couple (as well as advective and total torque couple, since these latter two are found to be of similar shape to the gravitational torque couple for self-sustained modes) in a single galaxy, and by implication multiple nested modes of differing pattern speeds, shows that the secular mass flow process is not a one-way street. During the lifetime of a galaxy a given radial range will experience inflows and outflows of different magnitudes, but there is an overall trend of the gradual central concentrating of matter together with the building up of an extended envelope, consistent with the entropy evolution direction of the self-gravitating systems. Galaxies accomplish this in a well-organized fashion, by first employing a dominant mode across the galaxy's outer disk, and subsequently with more of the modal activity moving into the central region of a galaxy, and the single dominant mode also bifurcates into multiple nested modes.

In Figure 18, we show the calculated radial gradient of gravitational torque coupling integral $dC_g(R)/dR$ as compared to the volume torque integral $T_1(R)$. There is about a factor of 3-4 difference between the $T_1(R)$ and $dC_g(R)/dR$ for most of the galaxies in the sample (for NGC 4736, this ratio in the inner region is as high as 8), indicating that the remainder, which is contributed by the gradient of the advective torque coupling, $dC_a(R)/dR$, is in the same sense but much greater in value than $dC_g(R)/dR$. Note that this difference between the volume torque integral and the gradient of the (surface) gravitational torque couple is only expected in the new theory: in the traditional theory of LBK these two are supposed to be equal to each other (see Appendix A2 of Z98).

Furthermore, if the LBK theory is used literally, one should not expect any mass flow rate at all over most of the galactic radii in the quasi-steady state, except at isolated resonance radii (since the total angular momentum flux, $C_a(R) + C_g(R)$, is expected to be constant independent of radius in the LBK theory). The existence of a mass flux across the entire galactic disk is thus also contrary to the LBK's original expectations, especially since there is strong evidence that the patterns in these same galaxies were steady modes (i.e., the fact we can use the potential-density phase shifts to successfully locate resonances in ZB07 and ZB09 shows that these patterns were steady modes).

We mention here that we have repeated the calculations for $dC_g(R)/dR$ and $T_1(R)$ using different scale height values. Even though both quantities are affected by a particular choice of the scale height, the relative ratios between the two quantities appear little affected. This is due to the fact that the potential that is being affected by the scale height choice enters into both the C_g and the $T_1(R)$ results, so their ratio is insensitive to the choice of scale height. So the conclusion of the significant difference between these two quantities at the nonlinear regime of the wave mode is robust.

The above result tells us that the correct treatment of gravitational many-body systems containing self-organized global patterns, such as density wave modes in disk galaxies, requires a re-examination of classical dynamical approaches

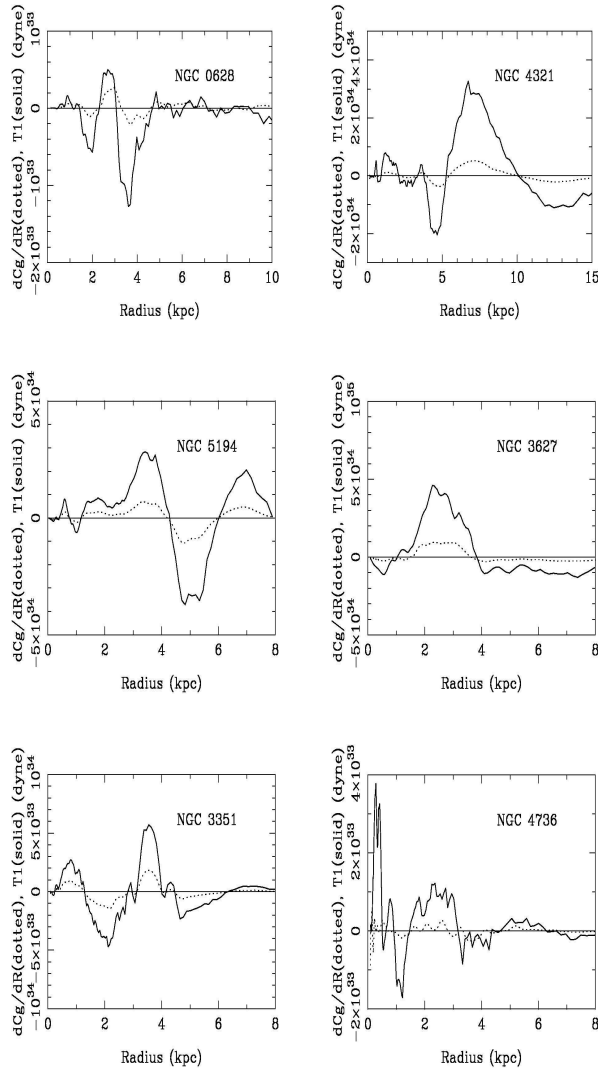


Figure 18. Radial gradient of gravitational torque coupling integral compared with the volume torque integral for the six sample galaxies. For NGC 0628, used IRAC 3.6 μm data; for NGC 4321, 3351, 3627, 5194, used the average of IRAC 3.6 μm and SDSS i-band data; for NGC 4736, used SDSS i-band data; to these the usual gas maps were added.

and assumptions. Our experience so far has shown that entirely new qualitative and quantitative results can emerge from the collective mutual interactions of the many particles in a complex dynamical system when the system is undergoing a dynamical instability or nonequilibrium phase transition. Formerly sacred laws (such as the differential form of the Poisson equation) can break down at the crest of collisionless shocks (Z98), and new meta-laws (such as the equality of the volume torque integral with the derivative of the sum of gravitational and advective surface torque coupling integrals) appear as emergent laws. Such emergent behavior is the low-energy Newtonian dynamical analogy of high energy physics' spontaneous breaking of gauge symmetry, a well known pathway for forming new meta laws when traversing the hierarchy of organizations.

In this context, we would like to elucidate further the relation of galactic collective effects with similar phenom-

ena in other classical and quantum systems. A terminology that is often used to describe this class of phenomena is *anomaly*. Wikipedia's definition for this term goes as follows: "In quantum physics an anomaly or quantum anomaly is the failure of a symmetry of a theory's classical action to be a symmetry of any regularization of the full quantum theory. In classical physics an anomaly is the failure of a symmetry to be restored in the limit in which the symmetry-breaking parameter goes to zero. Perhaps the first known anomaly was the dissipative anomaly in turbulence: time-reversibility remains broken (and energy dissipation rate finite) at the limit of vanishing viscosity".

From the above definition, we see that the existence of anomaly is associated with the symmetry breaking of the parent theory which is not a smooth continuation (or logical extension) of the underlying more symmetric theory (that was one of the reasons why the collective effects in the galactic density wave disk were never rigorously "derived" from the classical action-angle-based mean-field theory, and why so many "experts" of the old school have failed to realize these effects for many decades). In fluid turbulence (Firsch 1995 and the references therein), the amount of turbulence viscosity is not determined by microscopic viscosity of the fluid medium, but by energy injection and cascade from the largest scales. This feature has an analogous situation in galactic disks possessing density wave modes – the effective gravitational viscosity was determined solely by the modal parameters and not by the molecular viscosity in the underlying medium (a formal analogy of the density wave disk with a viscous accretion disk, including the derivation of effective gravitational viscosity parameters, was given in Z99, §2.1.1). It is also for this reason that the traditional distinction between the roles of stars and gas in the context of density-wave induced mass redistribution is so unnatural: In reality the viscosity in both mediums are dominated by the collective gravitational viscosity whose amount is determined by the self-consistency requirement of the large scale pattern.

Another characteristic associated with anomaly or symmetry breaking is the existence of singularity and closure relations. It is well-known that one-dimensional Burgers equation in fluid dynamics spontaneously develops a singularity in finite time if we evolve the solution from an initial singularity-free distribution (Burgers 1948). Similar situation in three-dimensional turbulence was analyzed by Onsager (1949). The analogy in galactic dynamics is that the Eulerian fluid description of galactic density waves (in the cylindrical or disk geometry) will spontaneously develop singularity at the wave crest in the nonlinear regime, if no viscosity is introduced. This spontaneous-steepening tendency of the nonlinear density wave is the basis for the formation of spiral collisionless shocks (§3.2 of Z96 and the references therein). The gravitational viscosity induced by the collisionless shock offsets the steepening tendency in the azimuthal direction, and the balance of the two leads to the closure relation, i.e. the volume torque relation which relates the total torque couple to the local angular momentum exchange rate between the basic state and the wave mode. The analogy of this phenomenon in quantum mechanics include the formation of axial anomaly (Schwinger 1951), whose description can be formally likened to the description of two-dimension turbulence (Polyakov 1993; Yen & Sreenivasan 2006). The

singularities formed in nonequilibrium phase transitions separate the different hierarchies of organization (as in spontaneous breaking of gauge symmetry), allowing older laws to cease to be valid and new laws (or meta-laws, as in our case the volume-torque closure relation) to take over as the emergent governing relations. Pfenniger (2009) also brought attention to the relevance of fluid turbulence analyses to the studies of galactic dynamics.

5.3 The Relative Contributions of Stellar and Gaseous Mass Flows

In the past few decades, secular evolution, bulge growth, and the evolution along the Hubble sequence were studied mainly within the framework of the secular redistribution of the interstellar medium under the influence of a barred potential, and the resulting growth of the so-called “pseudo bulges” (KK04 and the references therein). KK04 showed, however, that through gas accretion alone one could at most build late-type pseudobulges, but not intermediate and early type bulges, since the observed gas inflow rates and nuclear star-formation rates are both insufficient to account for the formation of earlier-type bulges through secular inflow of gas and the subsequent conversion of gas to stars during a Hubble time. Yet observationally, early type galaxies (including disk-Es) are known to form a continuum with the intermediate and late types in terms of the structural parameters and kinematics (Jablonka, Gorgas, & Goudrooij 2002; Franx 1993), and thus their formation mechanisms are also expected to be similar.

With the recognition of the role of collective effects in the secular mass redistribution process, the study of secular morphological transformation of galaxies should now give equal emphasis on the role of stellar and gaseous mass redistribution. Due to their different intrinsic characteristics (radial surface density distribution, compressibility, star-formation correlation, and dissipation capability), stars and gas do play somewhat different roles in the secular evolution process. In this subsection we illustrate with our sample galaxies some of the specifics of these roles.

In Figure 19 and 20, we present the comparison of stellar and gaseous (HI plus H₂) mass flow rates, as well as their respective phase shifts with respect to the total (star plus gas) potential. The phase shift plots tell us the relative efficiency of the stellar and gaseous mass accretion processes, since (from Z98, equation 25)

$$\frac{dL}{dt}(R) = \frac{1}{2} F^2 v_c^2 \tan i \sin(m\phi_0) \Sigma_0, \quad (9)$$

where $F^2 \equiv F_\Sigma F_V$ is the product of the fractional density and potential wave amplitudes, and m is the number of spiral arms (usually taken to be 2). Therefore, from equation (4), (5) in the current paper,

$$\sin(m\phi_0)_i = \frac{1}{\pi v_c R F_i^2} \frac{\frac{dM_i}{dt}}{(\Sigma_0)_i} \quad (10)$$

where the subscript i represent stars or gas, respectively. So for similar wave amplitudes between stars and gas, the mass component that has higher phase shift will have higher mass flow rate per unit surface density.

For galaxy NGC 0628, the stellar and gaseous accretion

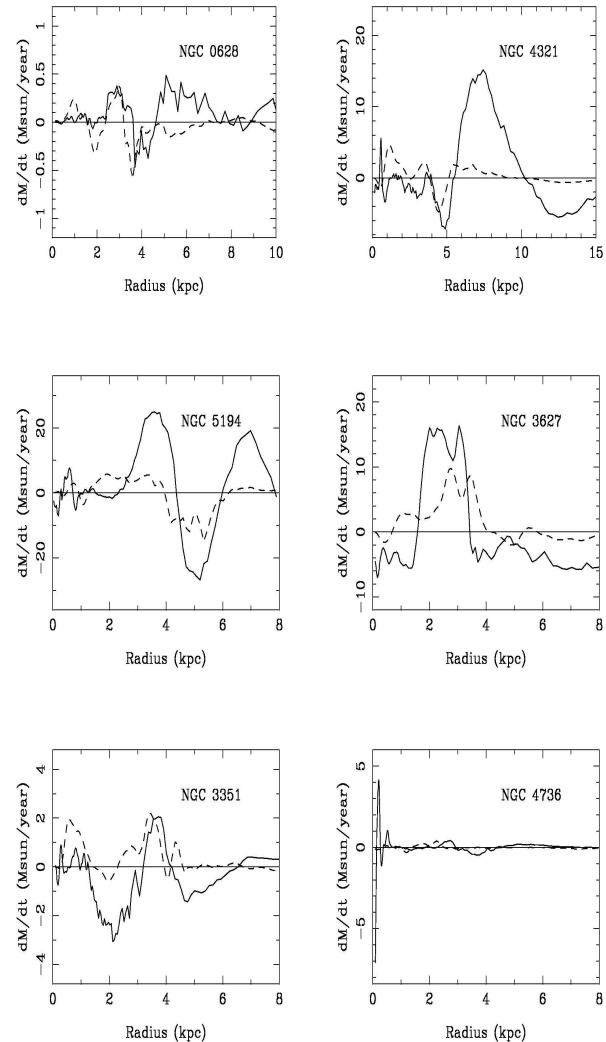


Figure 19. Stellar and gaseous mass flow rates for the six sample galaxies, calculated from the IRAC 3.6 μm for NGC 0628, an average of IRAC 3.6 μm and SDSS i-band for NGC 4321, 5194, 3627, 3351, and SDSS i-band for NGC 4736, plus VIVA, THINGS and BIMA SONG data. The total potentials used for these calculations were the same as previously derived using IRAC and/or SDSS for the stellar contributions, with appropriate averaging, plus the gas contributions.

efficiencies are similar, as are the respective total mass accretion rates, since this is a late-type spiral galaxy and is gas rich. The alignment of the stellar and gaseous phase shifts are not consistent, especially for the outer disk, indicating that the galaxy is yet to evolve into a state of dynamical equilibrium.

NGC 4321 is relatively quiescent and of intermediate Hubble type. From Figure 20, we see that for much of the central region (except the very center) the gaseous phase shift with respect to their common potential is much larger than the stellar phase shift, indicating that gas leads in phase in this region compared to stars, revealing the higher dissipation rate and thus mass redistribution efficient of the

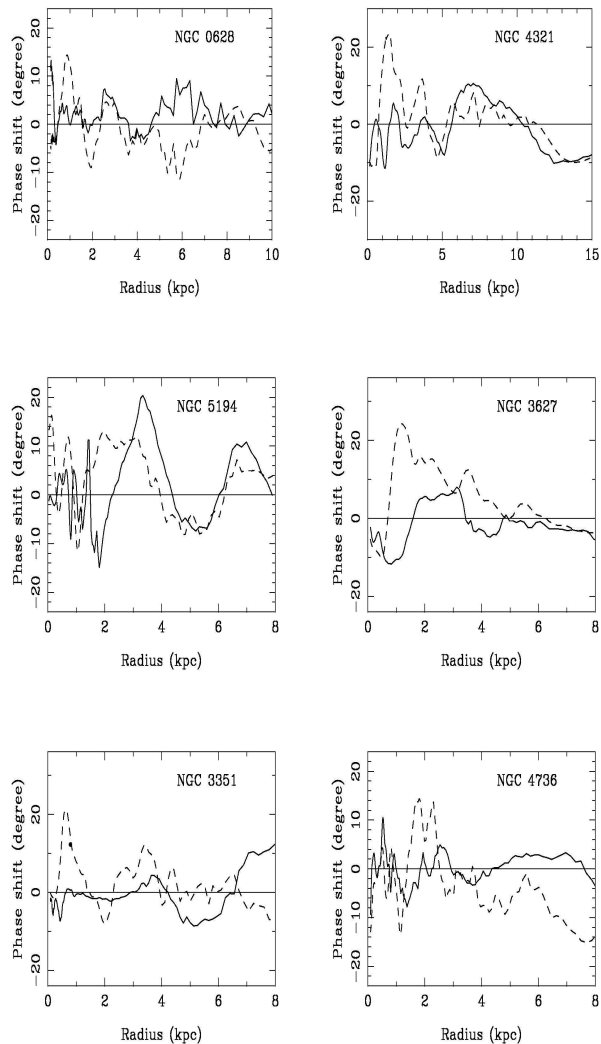


Figure 20. Stellar and gaseous phase shift with respect to total potential for the six galaxies. Solid lines: Stellar phase shifts. Dashed lines: Gaseous phase shifts. The stellar maps were derived using the IRAC 3.6 μm data for NGC 0628, using an average of IRAC and SDSS data for NGC 4321, 3351, 3627, 5194, and using SDSS i-band data for NGC 4637. The maps were from VIVA, THINGS and BIMA SONG observations. The total potentials used for these calculations were the same as previously derived using IRAC and/or SDSS for the stellar contributions, with appropriate averaging, plus the gas contributions.

gas compared to stars for the central region of this galaxy. The values of phase shifts of stars and gas are comparable for the outer region indicating that the two mass components have similar mass-redistribution efficiency there. The shapes of the positive and negative humps of phase shifts for stars and gas have more similar radial distributions for this galaxy compared to NGC 0628, especially for the outer region, indicating a higher degree of dynamical equilibrium. The overall contribution of the stars to mass redistribution, however, is much higher for stars than for gas in the outer region (Figure 19), because of the higher overall stellar surface density there.

Next the stellar and gaseous mass flow rates and phase shifts for NGC 5194 (M51) are presented. For this galaxy, unlike for NGC 4321, the stellar and gaseous phase shifts have significantly different radial distribution, even though both galaxies were of intermediate Hubble type. This indicates the non-dynamical-equilibrium state of M51 due to the tidal pull of the companion, and the inevitable evolution towards forming a new set of nested resonances, with the gas playing a leading role in seeking the new dynamical equilibrium because of its more dissipative nature, and the stellar component lagging somewhat behind in this action. But at every moment of this re-establishment of the dynamical equilibrium the overall density (i.e. the sum total of stellar and gaseous) still has a much more coherent phase shift distribution with respect to the total potential than each component considered separately (i.e. compared to Figure 8). The overall mass flow rate of stars is much higher than gas for this galaxy.

Next the stellar and gaseous mass flow rates and phase shifts for NGC 3627 are presented. For this galaxy, even though the phase shift in the central region shows that gas has a higher accretion efficiency than stars, the overall accretion rate of stars much exceeds those of gas. The second CR location is not shown here because of more limited radial range plotted, but is present in the total gas phase shift curve when examined further outward.

For the earlier-type galaxy NGC 3351, we see that the central region gas-star relative phase shift for this galaxy is even more severe than for NGC 4321. This is likely due to the fact that the straight bar potential in the central region of this galaxy is mostly contributed by stars, which has small phase shift with respect to the total potential, and gas thus contributes a much larger phase shift (through its dissipation in the bar potential and the phase offset of its density peak from the stellar density peak) to the overall potential-density phase shift. The overall mass flow rates are contributed similarly by stars and gas for this galaxy. Note that the somewhat chaotic appearance of phase shifts in the outer region of this galaxy is due to the low surface density there, and thus noise begins to dominate.

For NGC 4736, gas leads stars in part of the radial range, but the overall contribution to mass flow is mostly due to stars, especially for the central region, due to the fact that in this early-type galaxy the stellar surface density much exceeds that of gas. Also once again the low surface density in the outer disk of this early type galaxy leads to the more chaotic phase shift distribution there.

We see from this set of plots that some of the old myths, such as that the gas always torques stars inside and outside CR in the right sense, and from the change of sign of the relative phase between stellar and gaseous density distributions one can tell the CR location, is only true in small number of instances. To obtain a reliable CR estimate, one really needs to use the total density (star plus gas) and total potential, and calculation of the phase shift zero crossings between these two components to determine the CR locations. In the absence of the gas surface densities, stellar surface density alone and the potential calculated from it (as is done in ZB07), come as the next best compromise. Both of these approaches are much more reliable than if using the phase shift between the stellar density and gas density distributions. We also see that in the majority of the galaxies in the

local universe, secular mass flow is dominated by the stellar mass redistribution rather than by gas redistribution, unlike what has been emphasized by many of the earlier works on secular evolution.

We comment here that even for the gas accretion in disk galaxies, the mechanism responsible for its viscosity is still the collective gravitational instabilities (which manifests as the phase shift between the gas density and total potential), rather than the microscopic gaseous viscosity, which was long known to be inadequate both for the accretion phenomenon needed to form young stars, and for the accretion phenomenon observed in the gaseous disks of galaxies – thus the well-known need for anomalous viscosity in generalized accretion disks (Lin & Pringle 1987). Z99 showed that the large-scale density wave-induced gravitational viscosity is likely to be the source of anomalous viscosity in both the stellar and gaseous viscous accretion disks of galactic and stellar types.

5.4 The Relative Contributions of Atomic and Molecular Mass Flows

In Figures 21, we present the comparison of $H\text{I}$ and H_2 mass flow rates for our six galaxies. It is seen that for all five galaxies the H_2 mass flow follows more closely the stellar mass flow distributions, whereas the $H\text{I}$ has a more smooth and gradual distribution. This is likely to be a result of the process of the formation of molecular gas (and molecular clouds and complexes as well) at the spiral arms due to the density wave shock, and their subsequent dissociation. The $H\text{I}$ gas distribution, on the other hand, follows a more quiescent dynamics, even though a mild correspondence to the density wave patterns can be discerned. We emphasize that these plots should not be read as that the $H\text{I}$ gas is less responsive to the gravitational perturbation of the density wave than H_2 , but rather that when the response of the gas happens in the spiral shock, $H\text{I}$ will be converted to H_2 and thus will show up as H_2 in the response.

5.5 Implications on the Origin of Density Wave Patterns in Galaxies

Our current work has another important implication on the continuing debate regarding the modal-versus-transient nature of density wave patterns in disk galaxies (see, e.g., BT08 and the references therein). A recent contribution to this debate is Sellwood (2011), where N-body simulation results of spiral patterns based on the linear modal theory of Bertin et al. (1989), as well as on previous modal simulations by Donner & Thomasson (1994, hereafter DT94) and by Z96, Z98 are given. Sellwood (2011) concluded that the spiral patterns in his simulations are all transient waves rather than modes. While the cause for disagreement with the Bertin et al. theory may be due to the simplifying assumptions made in that theory, which are up to these authors to respond, in what follows we present our own response specific to Sellwood's comments regarding his repeat simulations of the DT94 and Z96,Z98 results (some of these text were extracted from earlier email exchanges between the first author and J. Sellwood).

- There is a significant distinction between the repeat

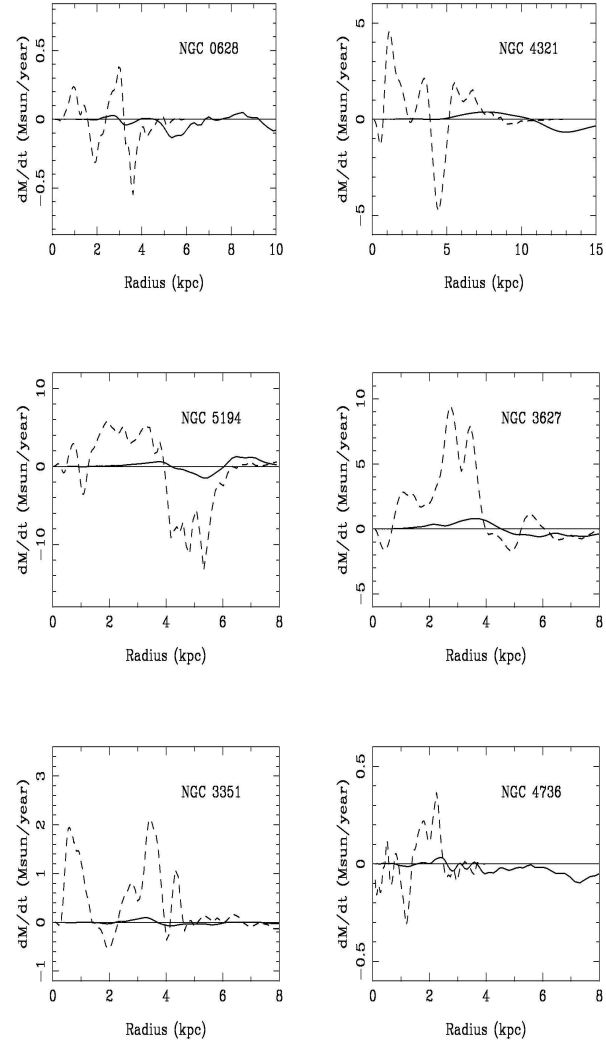


Figure 21. HI and H_2 mass flow rates for the six sample galaxies. Solid lines: HI mass flow rates. Dashed lines: H_2 mass flow rates. The HI mass flow rates were derived using mass maps from VIVA and THINGS observations, and H_2 flow rates were derived using mass maps from BIMA SONG observations. The total potentials used for these calculations were the same as previously derived using IRAC and/or SDSS for the stellar contributions, with appropriate averaging, plus the gas contributions.

simulations Sellwood conducted using the basic state specifications of DT94 and Z96, Z98, and those simulations he had done in the past for genuine transient spirals (see, e.g., Sellwood 2008 and the references therein). Almost all of his past simulations of transient spirals were carried out using basic states that were *over-stable* to the formation of spiral modes, and therefore the spiral patterns emerged in those disks were indeed transient wave trains. For barred galaxy simulations, such as in Sparke & Sellwood (1987), *unstable* basic states were on the other hand used, and these bar patterns formed were genuine bar modes. BZ09 had commented on the inconsistency of Sellwood's past practice in this regard, and pointed out that in realistic galaxies, such as the

more than 150 OSUBGS galaxies analyzed by us in the same paper, bars and spirals often co-exist in the same galaxy as nested patterns, it is not possible to specify the portion of the disk for bars as unstable to modal formation, and specify the portion of the disk for spirals as overstable for modal formation. In his 2011 paper, when Sellwood repeated the older simulations of DT94 and Z96, Z98, he had on the other hand used our basic state specification that is unstable for spiral mode formation – i.e. this is the first time Sellwood has simulated a galaxy disk that allowed the formation of unstable *spiral modes*.

- In Sellwood (2011)'s new simulations, he was able to reproduce the gross morphological features in our previous simulations. There is little question that the numerical codes we each used (in DT94, Z96, Z98, and Sellwood 2011) behaved similarly, apart from the larger number of particles used in the new simulations. The mere fact that the derived modal characteristics are nearly identical in both the old and the new simulations, shows that we indeed are all simulating **modes**, not transient waves. This is like someone plucking a guitar string: if the string length is held the same, no matter how much difference there is in the applied force, the fundamental mode excited has to be the same (i.e. the guitar will sound with the same basic tone). The same thing is true for disk galaxies: despite the unavoidable differences in the noise and random-variable performances of our various codes, the modal characteristics stay the same since the basic state characteristics (i.e. the radial distributions of surface density, random velocity and the rotation curve) are specified to be the same.

- Regarding the generating mechanisms of galactic density wave patterns, our view is that these are modes which are the fundamental instabilities of the basic state of the disk, whereas Sellwood thinks that they are transient waves regenerated on short time scales (Note that even Sellwood himself, during our private communication, had acknowledged that the mere fact that the power spectrum of the dominant spiral structure is coherent and spans much of the galactic radii means that its generating mechanism cannot be totally random. Yet he did not offer an alternative mechanism to the modal picture). In all other naturally occurring resonant systems, such as atmospheric convection (Benard instability), microwave resonant cavities, etc., unstable modes inevitably emerge if the boundary conditions allow them. In galaxies, the boundary condition naturally favors the appearance of modes: i.e., the disk would reach a marginally stable state for axisymmetric instabilities due to the self-regulating balance of gravitational and pressure forces. Then, when the disk is marginally stable to axisymmetric instabilities, it is unstable for bi-symmetric instabilities (spiral and bar modes). So for disk galaxies to spontaneously form these density wave modes is almost an unavoidable outcome. That is why these patterns appear to be so predominant in disk systems.

- Sellwood (2011) has pointed out that besides the dominant mode in the inner disk, which has its initial CR at 30 and OLR at 42 in Z96 and DT94's simulations, and which is 1/10 of these values in Sellwood's new simulation because of the different normalizations, there are spurious modes present at the same time. We agree with this conclusion of his. In fact, Figure 5 of DT94 showed other power spectrum peaks besides the main one (XZ has independently

confirmed this but did not present these results in the published papers), similar to what Sellwood has shown in his Figure 8 (though Sellwood identified a total of four modes, i.e., three spurious modes – a difference that is likely to be due to the difference in the detailed realization of our codes). However, these spurious power spectrum peaks (in the old as well as the new simulations) are all located in the outer region of the disk, where the surface density is extremely low, and the outer disk was not the main focus of our previous studies. Nonetheless, Figure 4 of Z98 (reproduced here as the top plot in Figure 1 of the current paper) did indeed show the presence of the first spurious edge mode as the second small bell hump. Z98 has limited the plotting region in that figure to $R=70$, therefore the third peak in DT94's Figure 5 in the extreme outer region of the disk does not show up. Due to the partial inter-penetration of the dominant and the spurious modes, beating and fluctuation of modal amplitudes do happen as Sellwood (2011) had commented. This had shown up in both Z98 and DT94's simulations (for example see Figure 2 in Z98 paper, or Figure 3 in DT94). So the recent simulations of Sellwood had not shown any qualitatively different results from our previous studies. Furthermore, the values of the power spectrum intensity in both DT94 and Sellwood (2011) was normalized to the surface density at each radius, and thus the outer peaks have much exaggerated amplitudes relative to the inner one, due to the low surface density in the outer disk, as Sellwood himself had also acknowledged in the same paper. In actuality the absolute amplitudes of these outer modes in the relevant simulations are very small in comparison with the absolute amplitude of the inner mode, which is precisely why the dominant spiral feature remains coherence for many pattern rotation periods in the Z98 simulation, with the spiral pattern lasting a significant fraction of a Hubble time. In physical galaxies (rather than this particular set of N-body simulations), the phenomenon of nested modes are of course common (see, e.g., ZB07 and BZ09). These modes generally have different pattern speeds, and these modes also emerge and transform in morphology as the basic state mass distribution evolves. So for a single basic state distribution there should in general be a compatible “modal system set” rather than a single mode, but such nested-modal-set is not the same as the random and transient wave trains that Sellwood is advocating.

- Regarding the dominant mode in that particular simulation (which has its OLR at 42 in our units, or 4.2 in Sellwood's units), Sellwood suggested that even this inner mode is itself composed of different appearing and disappearing transient waves. He argues for this from the vertical spread of the power spectrum in the last frame (sum of time history) of Figure 8 in Sellwood (2011). A hint about the reason of this spread, however, can be found from the two frames above the last frame: there one sees that the width of the power spectrum is a lot narrower after one divides the time history into two segments. This shows, that the real cause of the spread of power spectrum in the summed-history plot is that the modal characteristics are slowly changing in time as a result of the secular evolution of the basic state. This phenomenon can be made analogous to the growth of a human being from infancy to adulthood to old age. At each age-range the physical characteristics will be different. If one puts a stack of pictures of the individual at the different ages

side by side (similar to Sellwood's summed spectrum), one will see a spread of appearances. But the underlying person is the same one nonetheless, he/she is just going through the different evolution stages dictated by the programming of the genes (similar to the fundamental dynamical laws in galaxies plus the initial condition of galaxy formation), as well as by the environment he/she is brought up in (similar to the boundary conditions a galaxy will be experiencing in its lifetime). In the case of a person we do not say that he/she is constantly dying in the old self and constantly being regenerated in the new self (except as a way of speech), but rather a single person evolves from young to old (in the case of galactic density wave modes, this evolution includes the possibility of one mode evolving into nested multiple modes – but that process happens on longer timescale than what we are concerned about in establishing the quasi-steady nature of the spiral mode – for which we require the mode to be steady on local dynamical timescale). The analogy between the growth of a person and the evolution of galaxies in fact goes beyond superficial: Both the galaxies and the biological entities can be shown to be instances of the "dissipative structures" of I. Prigogine.

- Another piece of supporting evidence for the modal nature of galaxies is our recent work (ZB07; BZ09) on applying the potential-density phase shift method to determining the corotation radii in spiral and barred galaxies. For the phase shift method to be effective, the modes in question must have reached approximate quasi-steady state: otherwise the Poisson equation alone should not be able to be used to forecast kinematics properties. We found from analyzing the data for more than 150 nearby galaxies that the majority of them show good correspondence between the CRs determined by this method and the resonant features in galaxy images. The CRs determined by the phase shift method also agree well with that determined by TW method when there is only one primary CR in a single galaxy (as the TW method is most reliable in such instances), as well as with CRs determined by stellar isochrone methods of Martinez-Garcia et al. (2009, 2011).

- Regarding the dynamical mechanisms for secular evolution, Sellwood has made the claim that transient spirals are more effective than quasi-steady modes. This claim is erroneous. Z98 have shown that the secular mass flow rate due to collective effects produced by density wave modes depends mainly on the wave amplitude and on pattern pitch angle (which in turn determines the potential-density phase shift), and quasi-steady density-wave modes are extremely effective not only in terms of providing the correct sense of mass flow for bulge-building, but also in terms of soliciting the help of advective torques, which were shown in our current paper for observed galaxies, as well as in Z98 for simulated spiral modes, to be in the same sense of angular momentum transport as that of gravitational torques, and the total angular momentum transport is in fact dominated by the advective torques due to collisionless shocks. Similarly, quasi-steady modes had been shown to induce significant secular heating of the disk, and can explain the age-velocity dispersion relation of the solar-neighborhood stars (Z98, Z99) and the size-linewidth relation of the Galactic molecular cloud complexes (Zhang et al. 2001). The collective instabilities at the spiral arms are also expected to underlie the observed non-Schwarzschild distribution of Milky Way stars (Dehnen

1998), since the collisionless shocks completely decorrelate the phases of the otherwise regular orbits under the influence of smooth applied spiral potential. The mixing in the collisionless shocks could also explain the spread in metallicity for stars of a given age (since the spiral shock is on the order of 1 kpc in width as shown in Z96, thus leads to the mixing of stars and ISM from neighboring regions. The continuous inflow and outflow of matter due to successive nested resonances also facilitate the mixing process, and it does not require the presence of repeated transient wave trains as Sellwood had argued).

- Through our work using observed galaxy images, we found that in many instances the real physical galaxies in fact show a higher degree of coordinated behavior than the modes we were able to produce in N-body simulations. This shows up for example in the plots of the bell-shaped C_g versus R curves, which turn out to be in general much cleaner in observed grand-design galaxies than those in simulations. This we think is partially the result that observed galaxies have gone through a long history of natural evolution, so the degree of self consistency between the basic state and the modal characteristics is extremely good (at least for the grand-design ones). In simulations, we start the initial simulation somewhat abruptly (i.e. from a given axisymmetric basic state that does not contain a density wave mode that such a basic state should possess). And the subsequent boundary conditions enforced (that of a rigid bulge and halo in 2D simulations) are also artificial. So once again using the analogy of the growth of a human being, this is akin to a person born with a birth defect, and subsequently having to struggle in an environment that is not totally compatible with his natural inclinations. Such a person thus will never truly feel at ease throughout his life. Therefore, we should not take the results of simulations too literally. The appearance of spurious modes in these simulations could simply be a result of the unrealistic initial-boundary conditions assumed due to the limitations of computational facilities. The correct approach is to compare the results of these simulations and the results of observations with the aim to extract the essences of the underlying dynamical processes, going beyond the superficial spurious details.

- The conclusion of quasi-steady co-evolution of the basic state of the disk and the density wave modes is also supported by another aspect of our current work, which shows that for galaxies that are still at the initial stage of the secular evolution sequence, such as the case of the late-type galaxy NGC 0628, there is a poor coherence in both the phase shift plot as well as in the galaxy image, and poor correspondence between the phase shift zero crossings with any galaxy resonance features. As the galaxy settles down while the secular evolution proceeds, once galaxies reach intermediate Hubble types, such as galaxy NGC 4321, there is a very nice correspondence between the phase-shift-plot organization and the galaxy-image resonance organization, signaling that an internal dynamical equilibrium state has been reached. The delicacy of this balance (i.e., if we use an M/L-corrected *stellar image* alone without adding the gas maps in calculating the phase shift distribution, we would not get as well-organized phase shift curves as when we use the *total mass image*), shows that the equilibrium state is well negotiated between the mass distribution and the kinematic distribution of the density wave pattern, which

can only come as a result of the long-term evolution of spontaneously-formed density wave modes, and not possible for random transient wave trains. The observed correlation between basic state characteristics (i.e., the bulge-to-disk ratio) and pattern characteristics (i.e. the pattern pitch angle), already known at Hubble's time and is part of the basis of his classification scheme, is also most naturally explained within the modal framework (e.g., Bertin et al. 1989), at least qualitatively – even though the details of the modal theory may be challenged as Sellwood had shown in the first part of his 2011 paper.

To summarize, we note that to be able settle the question of transient versus modal nature of the density wave patterns in disk galaxies, we have to first be clear what we regard as a satisfactory definition of such a mode. We assert that a density wave is a mode if

- (i) It is a genuine instability in the underlying basic state of the disk.
- (ii) As a result it spontaneously emerges out of an originally featureless disk, for which the bell-shaped distribution of total angular momentum flux (or total torque coupling) of the mode is chiefly responsible (Z98).
- (iii) The properties of the emerged density wave patterns are determined solely by the basic state characteristics and not by the accidentals of noise.
- (iv) The emergence of these patterns greatly accelerates the entropy evolution of the parent basic state of the disk, as is the requirement for all dissipative structures formed in far-from-equilibrium systems.

Upon examining the evidence in both the simulated and observed disk galaxies possessing grand-design density wave patterns, we conclude that these patterns do conform to the definition of density wave modes as stated above. Furthermore, we emphasize that the modes in galaxies are indeed only quasi-steady, and not eternal and unchanging, since the secular mass flow they induce changes the basic state distribution, which in turn affects what kinds of modes are compatible with it. So these mode may change morphology continuously on time scales a few times of the local dynamical time scale (the exact rate of modal evolution differs depending on the density wave amplitude and pattern opening angle, etc., which will set the mass flow rates). In this context we once again bring out the connection with nonequilibrium phase transitions, and the fact that the coherent patterns formed in these transitions are in a state of dynamical rather than statical equilibrium.

Many of the more chaotic looking density wave patterns in late type disks, on the other hand, are likely to be in the process of evolving into grand-design ones due to the secular evolution connection among galaxies along the Hubble sequence as we are trying to establish in this paper.

5.6 Implications on the Secular Morphological Transformation of Galaxies

In the results presented so far, a picture emerges of the secular morphological transformation of galaxies driven mostly by collective effects mediated by large-scale density wave modes. This evolution is a well-coordinated quasi-steady evolution, with the formation and transformation of large-

scale density wave modes (through the formation of successive nested resonance patterns) in most circumstances compatible with the evolving basic state configurations.

The secular evolution mediated by the density wave pattern and its associated collective dissipation effect will slowly change the basic state mass distribution, but this change is accompanied by a corresponding change in the morphology, kinematics, and other physical properties of the density wave modes (including the formation of successive nested resonances), so at every state of the transformation from the late Hubble type to early Hubble type, there should be a good correspondence between the basic state properties and the density wave modes, except during the brief periods in a certain galaxy's life when they encounter gravitational perturbation from a companion galaxy, such is the case for M51 or NGC 3627, where it is seen that the coherence of the phase shift curves and the kinematic and dynamical equilibrium are temporarily disturbed. New equilibrium states are expected to be restored once the perturbation ceases and the galaxy adjusts its mass distribution and modal pattern to be once again mutually compatible – the reason these new equilibrium states are always possible is because for every basic state configuration there is almost always a set of unstable modes corresponding to it.

As a result of this coordinated co-evolution of basic state of the disk and the density-wave modes it supports, over the major span of a galaxy's lifetime the effective evolution rate depends on the stage of life a galaxy is in. Late- or intermediate-type galaxies, having larger-amplitude and open density wave modes in its outer disk, would lead to larger mass flow rates and thus secular evolution rates in the outer disk. Whereas for early type galaxies the secular evolution activity is shifted to the central region of a galaxy. In general the secular mass flow rate in the outer disks of early type galaxies are low, and this is reflected in the modal characteristics as well: i.e. early type galaxies generally have either tightly wrapped spiral arms, or straight bars, both correspond to small phase shift and thus small secular mass flow rate.

The secular evolution rate also depends on the interaction state of a galaxy, with the galaxy in group or cluster environments generally having larger evolution rates due to the large-amplitude, open spiral and bar patterns excited. Zhang (2008) showed that the interaction-enhanced, density-wave mediated evolution appear to underlie the so-called morphological Butcher-Oemler effect (Butcher & Oemler 1978) in rich clusters. Furthermore, there is the well-known morphology-density relation originally discovered by Dressler (1980), and subsequent shown to hold over more than 4 orders of magnitude in mean density spanning environments from field and groups, onward to poor clusters and rich cluster outskirts, all the way to dense cluster central region. The universality of such a correlation is in fact a powerful illustration of the unifying role played by “nurture-assisted-nature” type of processes during galaxy evolution. The dependence of morphology on environmental density shows that nurture plays an unquestionable role in determining the average evolution rate, yet the well-known inverse correlation of environmental density with merger rate shows that the effect of the environment is not chiefly in the form of violent cannibalism, but rather through mild tidal perturbations. Even the moderately-violent and episodic “ha-

rassment” type of direct damage to galaxy morphology is known to be ineffective at transforming the morphology of large disk galaxies: they are shown to mostly lead to the transformation of small disks to dwarf spheroidals (Zhang 2008 and the references therein). These leave the most obvious driver for the observed morphological transformation of galaxies in the different environments and the origin of the morphology-density relation as the tidally-enhanced density wave patterns operating over long times scales (though the time scale can be significantly shortened during strong tidal evolution which induce large-amplitude waves, and can thus enhance the evolution rate by a factor of several hundred times compared to galaxies in the quiescent environment – since the effective evolution rate due to the density waves depends on the wave amplitude squared).

However, as we see in the current work, even for interacting galaxies like M51 and NGC 3627, the environment exerts its effect through the innate mechanism already present in individual galaxies, i.e., the density wave modes that are excited during the interaction are still the intrinsic modes, the effect of interaction only enhanced the amplitudes of these modes.

The flip side of this correlation of evolution rate with environment is that some disk galaxies in isolated environments could have very small secular evolution rate throughout the span of a Hubble time, which explains the observational fact that many disk galaxies in the fields were found to have evolved little during the past few Gyr. Still, isolated environment cannot be automatically equated to a slow evolution rate. One of the most impressive examples of mass redistribution we have encountered is galaxy NGC 1530 (ZB07), which lies in a surprisingly pristine environment, i.e., nearly totally isolated. Yet NGC 1530 has by far the largest mass flow rate of all the galaxies we’ve calculated so far, on the order of more than 100 solar mass per year, due to its large surface density and the presence of a strong set of bar-spiral modal structure. This shows that the initial conditions that galaxies inherited at birth are likely to have played an important role as well in determining the subsequent morphological evolution rate.

The secular morphological transformation of galaxies along the Hubble sequence also implies that the required external gas accretion rate to sustain the current-level of star-formation rate in disk galaxies can be much reduced from the amount previously sought: As a galaxy’s Hubble type evolves from late to early, more and more of its store of primordial gas will be exhausted, and its star-formation rate will naturally decline. But this is precisely the observed trend of star-formation in galaxies along the Hubble sequence: i.e., the early-type disk galaxies do not have nearly as much star formation activity as late-type galaxies. Galaxies thus do not have to sustain their “current” level of star formation over cosmic time, since what’s current today will be history by the next phase of their morphological evolution.

A further inference is that as galaxies evolve from late to early Hubble types, the central potential well will gradually get deeper, and more and more intricate nested resonances form in the nuclear region as a result (Zhang et al. 1993). These successive resonances form a continued chain of mass fueling to the central region of a galaxy while the bulge itself grows, and this process could naturally account for

the observed correlations between the galaxy bulge mass and central black-hole mass.

Finally, we note that the continuous evolution across the S0 boundary into disk Es may erase the distinction between pesudo bulges and classical bulges, i.e., galaxies such as the Milky Way were previously thought to have classical bulges because of its $r^{1/4}$ central density profile, yet the building up of the Galactic Bulge is most likely through the secular mass accretion process over the pass 10 billion years, only that the disk bulge further relaxed into the $r^{1/4}$ shaped bulge with time. In the end, as has already been pointed out by Franx (1993), there might not be a clear distinction between early type disks and disk Es, and only a gradual variation of the bulge-to-disk ratio. The recent result from the ATLAS3D project of a significant disk component in all low-mass ellipticals (Cappellari et al. 2011) also supports this continuous evolution trend from late type disk galaxies all the way to disk Es.

6 CONCLUSIONS

In this paper we presented the study of a small sample of disk galaxies of a broad range of Hubble types in order to obtain an initial estimate of the radial mass accretion/excretion rates of these galaxies, to gauge the relevance of these processes to the secular morphological transformation of galaxies along the Hubble sequence. This study shows that the mass flow rates obtained in typical disk galaxies are able to produce significant evolution of their Hubble types over the cosmic time, especially if such disk galaxies have undergone external tidal perturbation, such as those encountered in group or cluster environment. We have found that the reasons past studies have concluded that secular evolution is only important for building up late-type pseudo-bulges are, first of all, the neglect of the important role of stellar mass accretion, and secondly, the neglect of the dominant role played by collective effects enabled by self-organized density wave modes. The recognition that a significant fraction of disk galaxies occupying the present-day Hubble sequence were built from a slow morphological transformation process implies that the composition of the dark halo of galaxies has to be mostly baryonic, a conclusion, though controversial in the context of the currently-popular LCDM paradigm, in fact naturally resolves many known paradoxes in this paradigm, such as the core-cusp controversy of low-surface-brightness galaxies, as well as the difficulty of cosmological simulations to form realistic disk galaxies when the material for disk formation is not made predominantly of baryons.

ACKNOWLEDGMENTS

We thank J. Sellwood, S. White and D. Pfenniger for helpful exchanges.

REFERENCES

- Alcock, C. et al. 1997, ApJ, 486, 697
- Bell, E. F. & de Jong, R. S. 2001, ApJ, 550, 212

Bell, E.F., McIntosh, D.H., Katz, N., & Weinberg, M.D. 2003, ApJS, 149, 289

Bershady, A., & Sreenivasan, K.R. 2003, Phys. Lett. A, 319, 21

Bertin, G., Lin, C.C., Lowe, S.A., & Thurstans, R.P. 1989, ApJ, 338, 78

Binney, J., & Tremaine, S. 2008, Galactic Dynamics, second ed. (Princeton: Princeton Univ. Press) (BT08)

Burgers, J.M. 1948, Adv. Appl. Mech. 1, 171

Buta, R. 1988, ApJS, 66, 233

Buta, R. & Combes, F. 1996, Fundamentals of Cosmic Physics, 17, 95

Buta, R., Corwin, H. G., de Vaucouleurs, G., de Vaucouleurs, A., & Longo, G. 1995, AJ, 109, 543

Buta, R.J., Vasylyev, S., Salo, H., & Laurikainen, E., 2005, AJ, 130, 506

Buta, R. & Williams, K. L. 1995, AJ, 109, 517

Buta, R.J., & Zhang, X. 2009, ApJS, 182, 559 (BZ09)

Buta, R. et al. 2010, ApJS, 190, 147

Butcher, H., & Oemler, A., Jr. 1978, ApJ, 219, 18; 226, 559;

Cappellari, M. et al. 2011, MNRAS, 416, 1680

Ceverino, D., Dekel, A., Mandelker, N., Bournaud, F., Burkert A., Genzel, R., & Primack, J. 2011, arXiv:1106.5587

Chemin, L., Cayatte, V., Balkowski, C., Marcellin, M., Amram, P., van Driel, W., & Flores, H. 2003, A&A, 405, 89

Chung, A., van Gorkom, J. H.; Kenney, J.D.P., Crowl, H., Vollmer, B. 2009 AJ, 138, 1741

Cimatti, A., Daddi, E., & Renzini, A. 2006, A&A, 453, L29

Clowe, D. et al. 2006, ApJ, 648, L109

Cohen, J.G. 2002, ApJ, 567, 672

Contopoulos, G. 1980, A&A, 81, 198

de Blok, W.J.G., 2010, AdAst 2010E, 5

Devereux, N.A., Kenney, J.D., & Young, J.S. 1992, ApJ., 103, 784

Dehnen, W. 1998, AJ, 115, 2384

de Grijs, R. 1998, MNRAS, 100, 595

Donner, K.J., & Thomasson, K., A&A., 290, 785 (DT94)

Dressler, A. 1980, ApJ, 236, 351

Eyink, G.L., & Sreenivasan, K.R. 2006, Rev. Mod. Phys. 78, 87

Firsch, U. 1995, Turbulence: The Legacy of A.N. Kolmogorov (Cambridge: CUP)

Flagey, N., Boulanger, F., Verstraete, L., Miville Deschénes, M. A., Noriega Crespo, A., & Reach, W. T. 2006, A&A, 453, 969

Foyle, K., Rix, H.-W., & Zibetti, S. 2010, MNRAS, 407, 163

Franx, M. 1993, in Proc. IAUS 153, Galactic Bulges, eds. H. Dejonghe & H.J. Hasinger (Dordrecht: Kluwer), 243

Fukugita, M., Hogan, C.J., & Peebles, P.J.E. 1998, ApJ, 503, 518

Genzel, R., Tacconi, L.J., Eisenhauer, F., Forster Schreiber, N.M., Cimatti, A., Daddi, E., Bouche, N. et al. 2006, Nature, 442, 786

Gnedin, O., Goodman, J., & Frei, Z. 1995, AJ, 110, 1105

Gunn, J.E. et al. 1998, AJ, 116, 3040

Haan, S., Schinnerer, E., Emsellem, E., Garcia-Burillo, S., Combes, F., Mundell, C.G., & Rix, H. 2009, ApJ, 692, 1623

Helfer, T. 2003, Thornley, M. D., Regan, M.W., Wong, T., Sheth, K., Vogel, S. N., Blitz, L.; Bock, D.C.-J. ApJS, 145, 259

Helou G. et al., 2004, ApJS, 154, 253

Hernandez, O., Wozniak, H., Carignan, C., Amram, P., Chemin, L., & Daigle, O. 2005, ApJ, 632, 253

Hopkins, P.F., Bundy, K., Murray, N., Quataert, E., Lauer, T.R., Ma, C.P., 2009, MNRAS, 398, 898

Jablonka, P., Gorgas, J., & Goudfrooij, P. 2002, Ap&SS, 281, 367

Jalocha, J., Bratek, L., Kutschera, M. 2008, ApJ, 679, 373

Jeans, J.H. 1928, Astronomy and Cosmology (Cambridge: CUP)

Kendall, S., Kennicutt, R. C., Clarke, C., & Thornley, M. 2008, MNRAS, 387, 1007

Kennicutt, R.C. et al. 2003, PASP, 115, 928

Koopmans, L.V.E., & De Bruyn, A.G. 2000, A&A, 358, 793

Kormendy, J., & Kennicutt, R.C. 2004, ARAA, 42, 603

Laurikainen, E. & Salo, H. 2002, MNRAS, 337, 1118

Lilly, S., Abraham, R., Brinchmann, J., Colless, M., Crampton, D., Ellis, R., Glazebrook, K., Hammer, F., Le Fevre, O., Mallen-Ornelas, G., Shade, D., & Tresse, L. 1998, in The Hubble Deep Field, eds. M. Livio, S.M. Fall, & P. Madau (Cambridge: CUP), 107

Lin, D.N.C., & Pringle, J.E., 1987, MNRAS, 225, 607

Lopez-Sanjuan, C., Balcells, M., Perez-Gonzalez, P.G., Barro, G., Garcia-Dabo, C.E., Gallego, J., & Zamorano, J. 2009, A&A, 501, 505

Lynden-Bell, D., & Kalnajs, A.J. 1972, MNRAS, 157, 1

Mahdavi, A., Hoekstra, H., Babul, A., & Balam, D.D. 2007, ApJ, 668, 806

Martinez-Garcia, E.E., Gonzalez-Lopezlira, R.A., Bruzual, A. G. 2009, ApJ, 694, 512

Martinez-Garcia, E.E., Gonzalez-Lopezlira, R.A., Bruzual, A. G. 2011, ApJ, 734, 122

McGaugh, S.S., Schombert, J.M., de Blok, W.J.G., & Zegers, M.J. 2010, ApJ, 708, L14

Meidt, S., et al. 2012, ApJ, 744, 17

Nelan, J.E. et al. 2005, ApJ, 632, 137

Nicol, M.-H. 2006, MPIA Student Workshop, http://www.mpia-hd.mpg.de/70CM/3rdworkshop/presentations/Marie-Helene_Nicol_dark_matter_SF_rate.pdf

Nicolis, G., & Prigogine, I. 1977, Self-Organization in Nonequilibrium Systems (NY: Wiley)

Onsager, L. 1949, Nuovo Cimento, Suppl. 6, 279

Ozernoy, L.M. 1974, in In: Confrontation of Cosmological Theories with Observational Data; Proc. IAUS 63 (Dordrecht: Reidel), 227

Peebles, P.J.E., & Yu, J.T. 1970, ApJ, 162, 815

Persic, M., & Salucci, P. 1992, MNRAS, 258, 14

Pfenniger, D. 2009, in Chaos in Astronomy, p.63 (Berlin: Springer)

Pfenniger, D., & Combes, F. 1994, A&A, 285, 94

Polyakov, A.M. 1993, Nucl. Phys. B, 396, 367

Quillen, A. C., Frogel, J. A., & Gonzalez, R. 1994, ApJ, 437, 162

Reach, W. T. et al. 2005, PASP, 117, 978

Sakharov, A.D. 1965, Zh.E.T.F., 49, 345

Schwarz, M. P. 1984, MNRAS, 209, 93

Schwinger, J. 1951, Phys. Rev. 82, 664

Sellwood, J.A., 2008, in Formation and Evolution of Galaxy Disks, Eds. J.G. Funes, S.J. and E.M. Corsini (SFO: ASP), 241

Sellwood, J.A., 2011, MNRAS, 410, 1637

Sellwood, J.A., & McGaugh, S.S. 2005, ApJ, 634, 70

Shostak, G.S., van Gorkom, J.H., Ekers, R.D., Sanders, R.H., Goss, W.M., & Cornwell, F.J. 1983, A&A, 119, L3

Shu, F.S. 1992, *The Physics of Astrophysics*, vol. II. Gas Dynamics, (Mill Valley, Univ. Sci. Books)

Sofue, Y. 1996, ApJ, 458, 120

Sofue, Y., Tutui, Y., Honma, A., Tomita, A., Takamiya, T., Koda, J., & Takeda, Y. 1999, ApJ, 523, 136

Sparke, L.S., & Sellwood, J.A. 1987, MNRAS, 225, 653

Sunyaev, R.A., & Zeldovich, Y.A.B. 1970, Ap&SS, 7, 3

Toomre, A. 1969, ApJ, 158, 899

Tully, R.B. 1974, ApJS, 27, 415

van Dokkum, P.G. et al. 2011, arXiv:1108.6060

Walter, F., Brinks, E., de Blok, W.J.G., Bigiel, F., Kennicutt, R.C.Jr., Thornley, M.D., Leroy, A. 2008, AJ, 136, 2563

White, S.D.M. 2009, in *Galaxy Disk in Cosmological Context*, Proc. IAUS 254, eds. J. Andersen, J. Bland-Hawthorn, & B. Nordstrom

Wolfe, A.M., Gawiser, E., & Prochaska, J.X. 2005, ARA&A, 43, 861

York, D.G. et al. 2000, AJ, 120, 1579

Zeldovich, Y.B. 1970, A&A, 5, 84

Zhang, X. 1992, Ph.D. Dissertation, University of California, Berkeley

Zhang, X. 1996, ApJ, 457, 125 (Z96)

Zhang, X. 1998, ApJ, 499, 93 (Z98)

Zhang, X. 1999, ApJ, 518, 613 (Z99)

Zhang, X. 2004, in "Penetrating Bars through the Masks of Cosmic Dust: The Hubble Tuning Fork Strikes a New Note", eds. D. Block et al., astro-ph/0406583

Zhang, X. 2008, PASP, 120, 121

Zhang, X. & Buta, R. 2007, AJ, 133, 2584 (ZB07)

Zhang, X., Lee, Y., Bolatto, A., & Stark, A.A. 2001, ApJ, 553, 274

Zhang, X., Wright, M.C.H., & Alexandria, P. 1993, ApJ, 418, 100

APPENDIX A. DESCRIPTIONS OF THE PROCEDURES FOR OBTAINING SURFACE MASS DENSITY MAPS

Stellar surface mass density maps can be made from two-dimensional images using surface colors as indicators of stellar mass-to-light ratio (Bell & de Jong 2001). Calibrated surface brightness maps can be converted to units of L_{\odot} pc $^{-2}$, and then multiplied by color-inferred M/L values in solar units to give the surface mass density $\Sigma(i, j)$ in units of M_{\odot} pc $^{-2}$ at pixel coordinate (i, j) . Thus our approach is two-dimensional and not based on azimuthal averages of the luminosity distribution.

It is widely regarded that the best images to use for mapping stellar mass distributions are infrared images, because these penetrate interstellar dust more effectively than optical images and also because such images are more sensitive to the light of the old stellar population that defines the backbone of the stellar mass distribution. For our study here, we used two principal types of images: (1) an Infrared Array Camera (IRAC) image taken at 3.6 μ m for the *Spitzer Infrared Nearby Galaxies Survey* (SINGS, Kennicutt et al. 2003); and (2) a 0.8 μ m *i*-band image obtained from the Sloan Digital Sky Survey (SDSS; Gunn et al. 1998; York et al. 2000). The pixel scales are 0. $''$ 75 for the 3.6 μ m im-

ages and 0. $''$ 396 for the *i*-band images. Only four of our six galaxies had SDSS data available. For NGC 3351 and 3627, the *i*-band images were rescaled to the scale of the 3.6 μ m images. For NGC 5194, the 3.6 μ m mass map was rescaled to the scale of the *i*-band to insure that the same area is covered on the two images.

Bell & de Jong (2001) give linear relationships between the log of the M/L ratio in a given passband and a variety of color indices in the Johnson-Cousins systems. Bell et al. (2003) give the same kinds of relations for SDSS filters. For the 3.6 μ m images of NGC 628, 3351, 3627, and 5194, we used $B - V$ as our M/L calibration color index, while for M100 we used $B - R$. For the SDSS *i*-band, we used $g - i$ as our main color. Using different color indices to scale the two base images from array units to solar masses per square parsec means that independent photometric calibrations are used, allowing us to examine effects that might be due to M/L uncertainties or systematics.

The base images we have used have different advantages and disadvantages for mass map calculations. For example, IRAC 3.6 μ m images have the advantages of much greater depth of exposure than most ground-based near-IR images and also they give the most extinction-free view of the old stellar background. Nevertheless, 3.6 μ m images are affected by hot dust connected with star-forming regions and by a prominent 3.3 μ m emission feature due to a polycyclic aromatic hydrocarbon compound that also is associated with star-forming regions (see Meidt et al. 2012). These star-forming regions appear as conspicuous "knots" lining spiral arms in 3.6 μ m images, such that the appearance of a galaxy at this mid-IR wavelength is astonishingly similar to its appearance in the *B*-band, minus the effects of extinction (e.g., Buta et al. 2010).

The advantages of the SDSS *i*-band are the shear quality of the SDSS images in general (especially with regard to uniformity of background), the reduced effect of star-forming regions compared to the *B*-band and the 3.6 μ m band, and the pixel scale which is almost a factor of two better than for the 3.6 μ m IRAC band. Nevertheless, extinction at 0.8 μ m is more than 40% of that in the *V*-band, so *i*-band images are considerably more affected by extinction than are 3.6 μ m images.

We use the 3.6 μ m and *i*-band mass maps as consistency checks on our results since neither waveband is perfect for the purpose intended. In practice, the star-forming region problems in the 3.6 μ m band can be reduced using an 8.0 μ m image if available (Kendall et al. 2008). These "contaminants" can also be eliminated using Independent Component Analysis (Meidt et al. 2012) if no 8.0 μ m image is available.

A1. Procedure

SDSS images - Images were downloaded from the SDSS archive using the on-line DAS Coordinate Submission Form. For the large galaxies in our sample, it was necessary to download multiple images per filter to cover the whole object (ranging from 3 for NGC 3351 to 9 for NGC 4736). These were mosaiced, cleaned of foreground and background objects, and then background-subtracted using routines in the Image Reduction and Analysis Facility (IRAF). SDSS images were available for 5 of the 6 sample galaxies, excluding NGC 628.

The zero points for the g and i -band images were obtained using information given on the SDSS DR6 field pages. The airmasses x_g and x_i , calibration zero points aa_g and aa_i , and extinction coefficients kk_g and kk_i , were extracted from this page and the zero points appropriate to the main galaxy fields were derived as

$$zp_g = -(aa_g + kk_g x_g) + 2.5 \log(a_{pix} t)$$

$$zp_i = -(aa_i + kk_i x_i) + 2.5 \log(a_{pix} t)$$

where a_{pix} is the pixel area equal to $(0.396)^2$ or $(0.75)^2$ if rescaled to the $3.6\mu\text{m}$ image and t is the integration time of 53.907456s. For the galaxies that were rescaled, we matched the coordinates of the SDSS g - and i -band images to the system of the $3.6\mu\text{m}$ image, which made it necessary to modify zp_g and zp_i to account for the new pixel size. This was done using IRAF routines GEOMAP and GEOTRAN. Foreground stars were selected that were well-defined on all three of the images. GEOMAP gave the rotation, shifting, and scale parameters, while GEOTRAN performed the actual transformations. Before the final transformations, the point spread function (PSF) of the images was checked. If the PSFs of the g - and i -band images were significantly different, the image with the best seeing was matched to the other using IRAF routine GAUSS. For M100, the higher resolution of the SDSS images relative to the $3.6\mu\text{m}$ image was retained.

The next step was to deproject these images in flux-conserving mode. For this purpose, IRAF routine IMLINTRAN was used with the adopted orientation parameters (see Table 1). When possible, we used kinematic orientation parameters for the deprojections. In the case of NGC 3351, we also used isophotal ellipse fits to deduce these parameters. No photometric decomposition was used for the deprojections; the bulges were assumed to be as flat as the disk.

The SDSS i -band mass map was derived as follows. The absolute magnitude of the Sun was taken to be $M_i = 4.48$ (CNA Willmer), with which the zero point needed to convert i -band surface brightnesses to solar i -band luminosities per square parsec is $zp_{\odot i} = 26.052$. To convert from these units to solar masses per square parsec, Bell et al. (2003) give a simple relationship:

$$\log \frac{M}{L_i} = -0.152 + 0.518(\mu_g - \mu_i)_o$$

where $(\mu_g - \mu_i)_o$ is the reddening-corrected $g - i$ color index. The only correction made was for Galactic reddening. This was judged using information from the NASA/IPAC Extragalactic Database (NED).³ Although NED lists extinction in the broad-band Johnson filters like B and V , it does not list the extinctions in g and i . To get these, the York Extinction Solver (YES; McCall 2004) was used on the NED website. The actual use of the above equation requires that some account be made of noise, because SDSS images are

³ This research has made use of the NASA/IPAC Extragalactic Database (NED), which is operated by the Jet Propulsion Laboratory, California Institute of Technology, under contract with the National Aeronautics and Space Administration.

not as deep as $3.6\mu\text{m}$ images. For our analysis, it is important to use the two-dimensional color index distribution, not an azimuthal average except in the outer parts of the disk where there is little azimuthal structure. Our procedure was to derive azimuthally-averaged surface brightness and color index profiles, and to interpolate colors from these profiles in the outer regions where noise made the actual pixel color too uncertain to be used in the above equation. Smoothing was also used even in intermediate regions. Usually, the colors in the inner regions were used without smoothing, and then annular zones of increasing radius used an $n \times n$ median box smoothing.

The median-smoothed raw i -band counts, $C_i(i, j)$, at array position (i, j) , were then converted to surface mass density $\Sigma(M_\odot \text{pc}^{-2})$ through

$$\Sigma(i, j) = C_i(i, j) \times 10^{-0.4(zp_i - A_i - zp_{\odot i})}$$

$$\times 10^{-0.152 + 0.518[\mu_g(i, j) - \mu_i(i, j) - A_g + A_i]}$$

The final SDSS mass maps usually would have left-over foreground stars that had not been removed, or dark spots in areas of star-formation where the color index was affected by too much blue light. These spots were removed using IRAF routine IMEDIT.

3.6μm Images - The procedure for these is in many respects similar to the procedure used for the SDSS images, except that different color index maps are used and these are not directly linked to the M/L ratio at $3.6\mu\text{m}$. For $3.6\mu\text{m}$ maps, we used $B - V$ or $B - R$ colors where the individual images are calibrated using photoelectric multi-aperture photometry. The sources and error analysis of such photometry, originally used to derive total magnitudes and color indices for RC3, are described in Buta et al. (1995) and Buta & Williams (1995).⁴ The typical uncertainty in the B -band zero point from this approach is 0.017 mag while for V it is 0.015 mag, based on 8-27 measurements. Fewer measurements are available for R -band calibrations from this approach; the uncertainties in these are described by Buta & Williams (1995). The B and V images used were downloaded from the SINGS database webpage. $B - R$ was used only for M100 and is based on images due to B. Canzian from observations with the USNO 1.0m telescope.

The surface brightnesses in the $3.6\mu\text{m}$ images were derived using a common zero point of 17.6935, based on the calibration from Reach et al. (2005). IRAC images are in units of MegaJanskys per steradian.

For our study here, we have made a “hot dust correction” to the $3.6\mu\text{m}$ images using a procedure similar to that outlined by Kendall et al. (2008) since all of our galaxies have an $8.0\mu\text{m}$ image available. The first step is to match the coordinate systems of the 3.6 and $8.0\mu\text{m}$ images and then subtract a fraction (0.232) of the $3.6\mu\text{m}$ flux from the $8.0\mu\text{m}$ image to correct the latter for continuum emission (Helou et al. 2004). Then, a fraction $R_{3.6/8.0}$ of the net dust map is subtracted from the $3.6\mu\text{m}$ map to give an image corrected for the hot dust emission. In general this method did improve our mass maps. The factor we used, $R_{3.6/8.0} =$

⁴ A full catalogue of UBV measurements may be found at <http://kudzu.astr.ua.edu/devatlas/revUBV.ecat.txt>.

0.059, is at the low end of the flux ratios found by Flagey et al. (2006) for the Galactic diffuse interstellar medium.

For converting $3.6\mu\text{m}$ surface brightnesses to solar luminosities per square parsec, the absolute magnitude of the Sun was taken to be $M_{3.6} = M_L = 3.27$ for the L -band, which is close to the same wavelength (Worley 1994). This corresponds to $zp_{\odot,3.6} = 24.842$. To convert from these units to solar masses per square parsec, two steps are used. The first is to derive the K -band M/L ratio from the corrected broadband colors. For $B - R$, the relation used is (Bell et al. 2003):

$$\log \frac{M}{L_K} = -0.264 + 0.138(\mu_B - \mu_R)_o$$

where $(\mu_B - \mu_R)_o$ is the Galactic reddening-corrected color index based on extinctions listed in NED. This relation differs substantially from that for the same color and near-IR band listed in Table 1 of Bell & de Jong (2001), which Bell et al. (2003) suggest is due to a larger metallicity scatter than accounted for in the earlier paper.

The second step is to convert $\frac{M}{L_K}$ into $\frac{M}{L_{3.6}}$. We used a simple relation due to Oh et al. (2008), based on stellar population synthesis models with a range of metallicities and star formation histories;

$$\frac{M}{L_{3.6}} = 0.92 \frac{M}{L_K} - 0.05$$

Because of the higher signal-to-noise in the $3.6\mu\text{m}$ image, it was not necessary to use the staggered median smoothing approach used for the SDSS images. The surface mass densities were then derived from the array values $C_{3.6}$ using

$$\begin{aligned} \Sigma(i,j) &= C_{3.6}(i,j) \times 10^{-0.4(zp_{3.6} - A_{3.6} - zp_{\odot,3.6})} \times \\ &0.92(10^{-0.264+0.138[\mu_B(i,j) - \mu_R(i,j) - A_B + A_R]}) - 0.05 \end{aligned}$$

For those cases where $B - V$ was used instead (NGC 628, 3351, 3627, and 5194), the M/L relation applied was (Bell et al. 2003)

$$\log \frac{M}{L_K} = -0.206 + 0.138(\mu_B - \mu_V)_o$$

where against the Galactic extinction corrections were taken from NED.

Addition of gas - Our analysis requires total mass maps, and thus it is essential to add in the contributions of atomic and molecular gas. Five of our sample galaxies were observed in The HI Nearby Galaxy Survey (THINGS; Walter et al. 2008), while M100 was observed as part of the VLA Imaging of Virgo Spirals in Atomic Gas (VIVA) program (Chung et al. 2009). All 6 are included in the BIMA Survey of Nearby Galaxies (BIMA SONG, Helfer et al. 2003). VIVA provides an HI image with resolution $31'' \times 28''$ and pixels $10'' \times 10''$. THINGS provides HI maps with a resolution of $\approx 6''$ and pixels $1''.5$ in size. The maps in all cases are publicly available, and the procedure for adding both HI and CO into the mass maps was the same. For the HI map, the total flux in the image was integrated to a radius consistent with the HI size of the object using IRAF routine PHOT. The map was then scaled to the measured total flux S_{HI} given

in Table 5 of Walter et al. (2008) and in Table 3 of Chung et al. (2009). With this scaling, each pixel in the image then has the same units, Jy km s^{-1} , and can be converted to mass using $M_{HI}(i,j) = 2.36 \times 10^5 D^2 S_{HI}(i,j)$, where D is the distance in Mpc. Dividing each value by the number of square parsecs in a pixel, this gives the distance-independent surface mass density of HI gas in units of $M_\odot \text{ pc}^{-2}$.

For the CO map, Table 4 of Helfer et al. (2003) gives the global CO flux, S_{CO} , for each galaxy. The same procedure as for the HI map gives the scaling of each pixel, such that the mass in each pixel is $M_{H_2}(i,j) = 7845.0 D^2 S_{CO}(i,j)$, where a conversion factor of $X = 2 \times 10^{20}$ has been used (Helfer et al.). The scale of the publicly available images is $1''.0$ per pixel.

The pixel sizes of the two gas maps were different from the pixel sizes of the $3.6\mu\text{m}$ and i -band images. IRAF routine IMLINTRAN was used to create scaled maps with the same pixel sizes, outputted to an appropriate center of the galaxy. Each paper gave the right ascension and declination of the pointing center, which was compared with the coordinates in the RC3 to judge where we should set the centers in our mass maps. Each scaled map had its own flux-scale factor to keep the total masses the same as published by Helfer et al. (2003), Walter et al. (2008), and Chung et al. (2009).

Gravitational Potentials - The potentials were calculated using the 2D Cartesian approach outlined by Binney & Tremaine (2008) as described in ZB07 (and similar to the approach used by Quillen et al. 1994). An important parameter needed in this calculation is the vertical scale height, assuming an exponential vertical density distribution. We used the approximate radial scalelengths listed in Table 1 and information from de Grijs (1998) to judge scale heights. Being bright galaxies, there are other sources of radial scalelength determinations for our sample. A literature search showed good agreement between our estimated values and other sources except for NGC 4736, whose complex structure causes a large spread in values, and for NGC 5194, which is complicated by its companion.

Uncertainties in mass map determinations and derived results - The uncertainties in our mass maps come from a variety of sources. In general, photometric calibration uncertainties are small, and less than 0.05 mag. The principal uncertainties come from the M/L calibrations, effects of dust, and from deprojection and orientation parameter uncertainties. According to Bell et al. (2003), typical uncertainties in a color-dependent M/L involving a near-IR band (such as M/L_K) is ± 0.1 dex for redder $B - V$ and $B - R$ colors, and ± 0.2 dex for bluer colors. We have shown that the Bell et al. (2003) $B - V/B - R$ calibrations with $3.6\mu\text{m}$ as the base stellar mass image give azimuthally-averaged radial surface mass density profiles very similar to those given by the Bell et al. (2003) $g - i$ calibration with the i -band as the base stellar mass image. From comparisons between the two base images and using also the Bell & de Jong (2001) $B - V/B - R$ calibrations, we found that phase shift distributions are more robust to M/L uncertainties than are mass flow rates, although even the latter agree fairly well between the two base images.

On the issue of orientation parameters, we did not experiment with different values but simply point to section 5.2 of BZ09 where tests were made of the impact of such uncertainties, including problems of bulge deprojection. The

CR radii we list in Table 2 are for the assumed orientation parameters in Table 1.

Uncertainties in the assumed vertical scale-heights were examined for M100. Reducing h_z from $12''.6$ in Table 1 to $3''.8$ had almost no effect on the phase shift distribution. In the outer disk near 7 kpc, the flow rate is increased by about 10% but at 1 kpc the difference is about 30%. Thus even a drastic difference in h_z has only a relatively small effect on our results.

The issue of dust enters in the uncertainties in two ways: through the significant impact of dust on the optical M/L calibrating colors, and through the “hot dust correction” to the $3.6\mu\text{m}$ image. The former is less of a problem than might be thought. As noted by Bell et al. (2003), the effects of dust approximately cancel out to 0.1-0.2 dex when estimating color-derived M/L values because, in most passbands, stellar populations and dust predict about the same amounts of reddening per unit fading. That is, while dust reddens the starlight, redder colors imply higher M/L , which effectively can reduce the impact of dust lanes. Our results here basically verify this point. The uncertainty in the hot dust correction lies mainly in the factor $R_{3.6/8.0}$. We chose a low end value from Flagey et al. (2006) for this correction, but higher values may be appropriate for some galaxies (e.g., Kendall et al. 2008).

APPENDIX B. CATEGORIES OF BAR-SPIRAL MODAL MORPHOLOGY

In this appendix, we give the schematics of the phase shift distributions of the various types of bar-spiral morphology, followed by examples of real galaxies that we have analyzed in BZ09. The sequence we present with these examples agrees roughly with the order of Hubble sequence from late to early, in order to show possible evolutionary connections between the various morphological patterns.

In Figures 22 and 23, we present the schematic and an example of a slow bar. These bars are characterized by the fact that the bar ends within CR, with possible spiral structure emanating from the bar ends. The hosts are predominantly late-type galaxies, with a significant flocculent pattern in the outer regions. Closer inspection of the phase shift plot for NGC 3686 shows that around the location of the bar end, a new phase shift P/N transition is in the process of forming. Thus the slow bar appears to be a short-lived phase in the process of evolving into bar-driven spirals, which we will analyze next.

In Figures 24 and 25, we present the schematic and an example of fast bars with coupled spirals, commonly referred to as bar-driven spirals. These patterns most often appear in intermediate-type galaxies, and the bar-driven spiral appears to have evolved through stages of either a slow bar or else a skewed long bar.

In Figures 26 and 27, we present the schematic and two examples of fast bars with decoupled spirals. On the one hand, these appear to be the further evolutionary stage of a bar-driven spiral, with the inner bar decoupled from the outer spirals and with the bar end coinciding roughly with the CR radii. The signature of the decoupling (at the N/P phase shift crossing) shows up as branching of the spiral arms disconnected from the bar-end. Close inspection of the

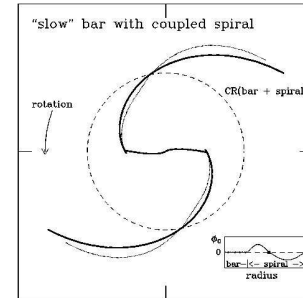


Figure 22. Schematic of the phase shift distribution for the slow bar.

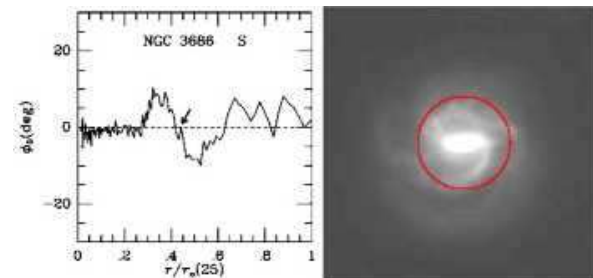


Figure 23. Examples of the phase shift distribution and morphology for the slow bar

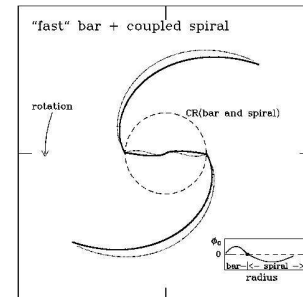


Figure 24. Schematic of the phase shift distribution for the fast bar with coupled spiral pattern.

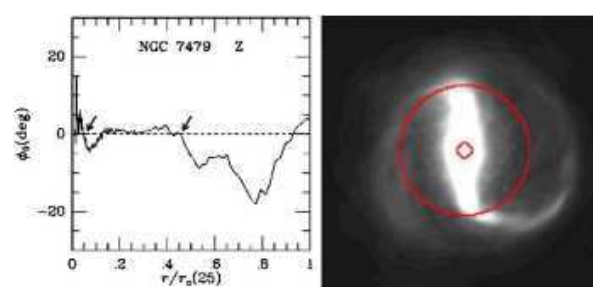


Figure 25. Examples of the phase shift distribution and morphology for the fast bar with coupled spiral pattern.

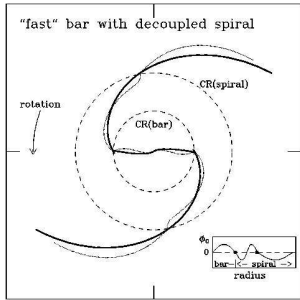


Figure 26. Schematic of the phase shift distribution for the fast bars with decoupled spiral pattern.

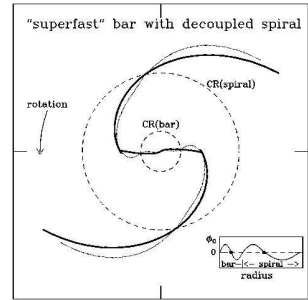


Figure 28. Schematic of the phase shift distribution for the super-fast bars with decoupled spiral pattern.

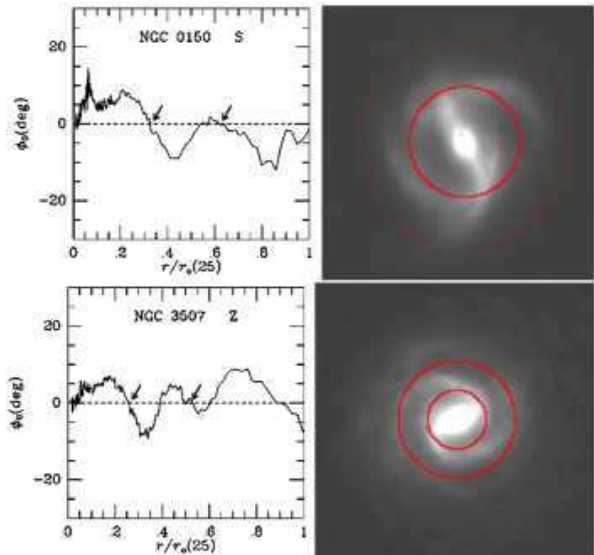


Figure 27. Examples of the phase shift distribution and morphology for the fast bars with decoupled spiral pattern.

images and the phase shift plots show that the two examples we give will evolve into somewhat different configurations later on: NGC 3507 appears to be evolving towards an inner bar-driven spiral followed by an outer spiral, whereas, NGC 0150 appears to be evolving towards superfast bar with decoupled spiral that we will discuss next.

In Figures 28 and 29, we present the schematic and an example of the so-called super-fast bars with decoupled spirals. The phrase super-fast bars are used to denote the fact that the bars extend significantly beyond their CR radii. In ZB07, we have shown a case of a single isolated bar in the galaxy NGC 4665, where the bar ends extend about 10–20% beyond the CR radius, and argued that in this case it is reasonable to expect the bar to be longer than the CR radius because the SWING amplified over-reflected waves from the inner disk must penetrate CR into the outer disk as transmitted wave in order to have the overall angular momentum budget balance. In our current plot, the super-fast section of the bars are straight segments emanating from the location of an inner oval. The end of the bar coincides not with CR but with the next N/P phase shift crossing after the CR. This is reasonable because modal growth re-

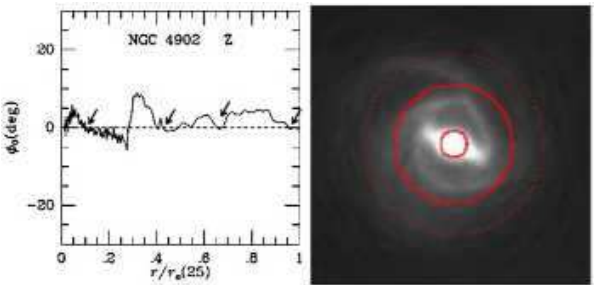


Figure 29. Examples of the phase shift distribution and morphology for the super-fast bars with decoupled spiral pattern.

quires that for a complete self-sustained mode there must be a positive phase shift packet followed by the negative phase shift packet, with the two packets joining at CR. This is because the density wave/mode has negative energy and angular momentum density inside CR (Shu 1992), and for its spontaneous growth the potential must lag the density – which leads to the positive potential-density phase shift – in order for the wave to torque the disk matter in the correct sense to lead to its own spontaneous growth by losing angular momentum to the disk matter. Vice versa for the modal content outside CR. Therefore we see that for the kind of twin-bars joining the central oval the mode has little choice but to have the N/P phase shift crossing be at the end of the bar.

Evidence supporting the claim that an N/P crossing is the location where the modal pattern speed changes discontinuously is that there is a pronounced ring-like structure at the radius of the N/P crossing, obviously caused by the snow-plough effect of the interaction of the inner and outer modes. Similar configuration of a central oval joined by straight super-fast bars are also observed in NGC 3351, NGC 1073, NGC 5643, and in the central region of NGC 4321. As a matter of fact, since this configuration requires the central oval connecting to the straight bars, it is always found in the central configuration of the nested modes.

Comparing the last two types of morphologies, we can clearly see that the fast-bars-with-decoupled-spirals appear to be evolving into super-fast-bars-with-decoupled spirals (i.e., in the phase shift plot for NGC 0150 we see that a new P/N crossing at the end of inner oval in in the process of forming, or dropping down to zero. When it is fully formed this will become a super-fast bar.

It is no coincidence that the super-fast bars, which often appear in early type galaxies, have a more rounded nuclear pattern and very straight two segment of bars connecting to it: both of these patterns are not much skewed and they correspond to very small phase shift, and slow secular evolution rate as befits the early type galaxies. The fact that bar-driven spirals mostly have skewed nuclear bar patterns followed by trailing spiral segments that taper into narrow tails, whereas super-fast bars most often have rounded nuclear patterns followed by very straight bar segments which broaden into dumb-bell shaped pile-up of material at the mode-decoupling radii shows that super-fast bars are real, and are of completely different modal category than bar-driven spirals.

Note that these four categories are the main types of bar-spiral associations, but they do not exhaust all the morphological types encountered in real galaxies. For example, the above categories did not include the cases of either pure spiral (i.e. NGC 5247 analyzed in ZB07), or pure bar (i.e. NGC 4665 also analyzed in ZB07).

From the above analysis we see that distinctive phase shift patterns seem to delineate distinctive galaxy morphology proto-types, with the morphology of galaxies within a type category repeatable to a high degree. These morphological features also seem to correlate with the Hubble types of the basic state of the galactic disks (i.e., its being early, intermediate, or late). These correlations are naturally explained under modal theory of density wave patterns since the density wave modal morphology are determined by the basic state characteristics (i.e., the radial distribution of surface density, rotation curve, and velocity dispersion in galaxy). The fact that the PDPS method can consistently pick out the given set of modal morphology and classify its resonance structure shows that its success is not an accident, but rather supported by the underlying modal structure of the density wave patterns.